Electronic Structure of Ru Nanosheets Studied by Photoemission and Inverse Photoemission Spectroscopies

K. Kodera [a], D.Ootsuki [a], D. Shibata [a], M. Kawamoto [a], D. Shimonaka [a], S. Yamamoto [a], M. Kobayashi [b], H. Kumigashira [b], K. Fukuda [c], S. Toyoda [d], Y. Uchimoto [a], H. Sato [e], M. Arita [e], H. Namatame [e], M. Taniguchi [e], and T. Yoshida [a]

[a] Graduate School of Human and Environmental Studies, Kyoto University, Sakyo-ku, Kyoto 606-8501, Japan
[b] KEK, Photon Factory, Tsukuba, Ibaraki 305-0801, Japan
[c] Office of Society-Academia Collaboration for Innovation, Kyoto University, Sakyo-ku, Kyoto 606-8501, Japan
[d] Department of Materials Science and Engineering, Kyoto University, Sakyo-ku, Kyoto 606-8501, Japan
[e] Hiroshima Synchrotron Radiation Center, Hiroshima University, Higashi-Hiroshima, 739-0046, Japan

Since the discovery of graphene, a considerable number of studies have been conducted on atomic monolayer materials. Recently, Fukuda *et al.* have succeeded to synthesize Ru nanosheets using a topotactic reaction [1-2]. Interestingly, the absorption spectroscopy of Ru nanosheets shows that the absorbance strongly depends on the number of layers, indicating the suppression of conductivity with decreasing the number of layers.

In this study, we have performed inverse-photoemission and high-resolution photoemission spectroscopy measurements in order to reveal the mechanism of the metal to insulator transition of Ru nanosheets (1, 6 and 9 L) on Si substrate. The inverse-photoemission spectroscopy (IPES) measurement was carried out using the IPES spectrometer with the tunable-photon energy (TPE) mode at Hiroshima Synchrotron Radiation Center (HSRC). The total energy resolution was 1240 meV for the incident electron energy 60 eV. The vacuum-ultraviolet photoemission spectroscopy (PES) measurement was carried out at BL-9A of HSRC. The total-energy resolution was 16 meV for hν = 20 eV. The sample surface of Ru nanosheets (1 and 9 L) were cleaned *in situ* by annealing at 300 ℃ for 15-30 min. The Fermi level was calibrated using the Fermi edge of the gold reference samples.

Figure 1 shows the IPES spectra of Ru nanosheets compared with soft x-ray photoemission (SXPES) spectra of Ru nanosheets (Fig. 1 (a)) taken at Photon Factory BL-2A. The IPES spectra of the 9 L sample exhibits a clear Fermi-edge, consistent with that of the SXPES spectra. On the other hand, the spectral weight at E_F for the 1 L sample is suppressed compared to the spectra of the 9 L sample, corresponding to the gap formation observed in the SXPES spectra. Moreover, these results are also observed in the high-resolution PES spectra as shown in Fig. 2 (a).
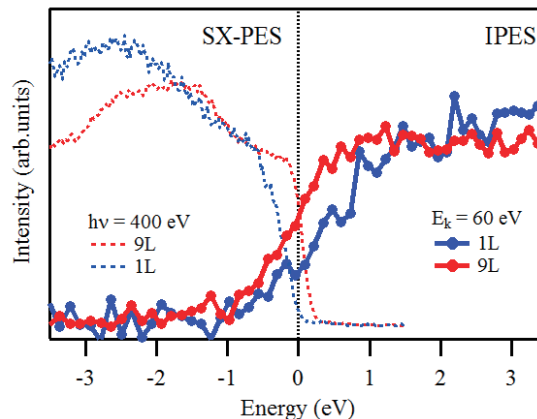
FIGURE 1. IPES spectra and SXPES spectra of Ru nanosheets (1 and 9 L).

In order to investigate the gap behavior near E_F, we plot the high-resolution PES spectra on a logarithmic scale in Fig. 2 (b). In the 1 L sample, the spectral weight near E_F shows the unconventional soft gap and follows a scaling rule proposed by Shinaoka and Imada [3], where the density of states A(E) follows a scaling in energy E as A(E) exp[-(-γlog|E-E_F|)^d]. Therefore, the present result suggests that the soft gap in the 1 L sample is driven by the coexistence of the short-range Coulomb interaction and disorder.
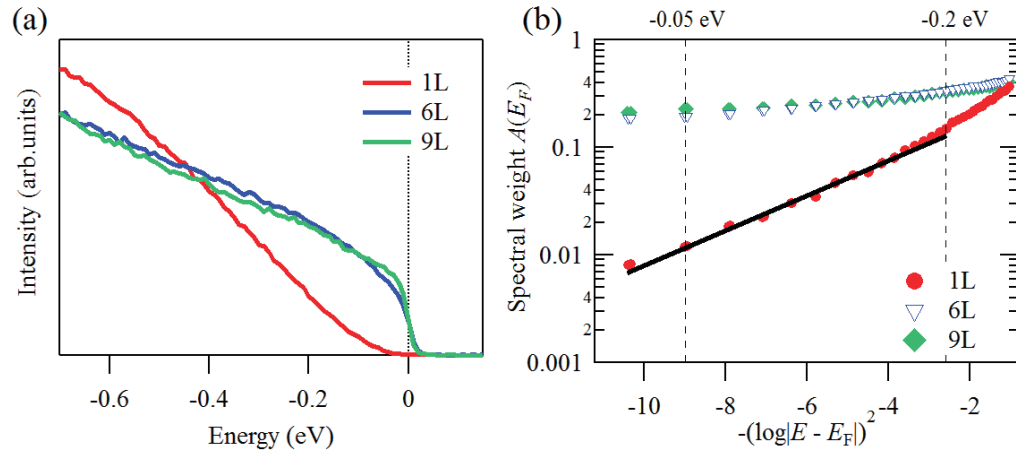
FIGURE 2. (a) High-resolution PES spectra of Ru nanosheets (1, 6, and 9 L) taken at hν =20 eV. (b) Logarithmic scale plot of the PES spectra. We show that there exist unconventional soft gaps,

REFERENCES

1. K. Fukuda *et al.*, Inorg. Chem. **52**, 2280−2282 (2013).
2. S. Toyoda *et al.*, Chem. Mater. **28**, 5784−57902 (2016).
3. H. Shinaoka and M. Imada, Phys. Rev. Lett. **102**, 016404 (2009).

Electronic Structure of $Ca_{2-x}Sr_xRuO_4$ (x=0.06) in Mott Insulating Phase Studied by Photoemission and Inverse Photoemission Spectroscopy

D. Shibata[a], M. Kawamoto[a], D. Ootsuki[a], C. Sow[b], Y. Maeno[b], F. Nakamura[c], H. Sato[d], H. Namatame[d], and T. Yoshida[a]

[a]*Graduate School of Human and Environmental Studies, Kyoto University, Kyoto 606-8501, Japan*
[b]*Department of Physics, Graduate School of Science,, Kyoto University, Kyoto 606-8502, Japan*
[c]*Kurume Institute of Technology, Fukuoka 830-0052, Japan*
[d]*Hiroshima Synchrotron Radiation Center, Hiroshima University, Higashi-Hiroshima 739-0046, Japan*

Keywords: Mott Insulator, Ruthenate,

A t_{2g}-electron system $Ca_{2-x}Sr_xRuO_4$ with a layered perovskite structure shows a rich phase diagram [1,2]. Sr_2RuO_4 is a leading candidate of spin triplet superconductor. On the other hand, Ca_2RuO_4 is an antiferromagnetic insulator below $T = 110$ K and a paramagnetic insulator between $T = 110$ K and 357 K. Since $Ca_{2-x}Sr_xRuO_4$ exhibits the coexistence of the metallic transport and the local magnetic moments, and the heavy fermion behavior in the region $0.2 \leqq x \leqq 0.5$, the scenario of orbital-selective Mott transition has been proposed by Anisimov *et al.*[3]

In this work, we have studied the electronic structure of $Ca_{2-x}Sr_xRuO_4$ (x = 0.06) in the insulating phase using photoemission spectroscopy (PES) and inverse-photoemission spectroscopy (IPES). Figure 1 shows the PES and IPES spectra, compared with the LDA calculation in the paramagnetic insulating phase. The shoulder structure at 1 eV and the peak structure at -0.8 eV correspond to the upper and lower Hubbard bands. A broad peak structure around 4 eV and 9 eV are derived from the Ru *4d* e_g orbitals and Ca *4s*, respectively. Figure 2 shows angle resolved photoemission spectra (ARPES) taken at hv = 23 eV. The O *2p* band dispersions have been observed in the energy region 3-6 eV below E_F. The parabolic band dispersion and the lower Hubbard bands are observed from E_F to -3 eV. In order to determine the orbital character of these band dispersions, we show the ARPES spectra taken by using *s*- and *p*- polarized light as shown in Fig. 2 (b) (c). The polarization dependence and band calculation reveal that the peak at ∼ -0.8 eV and ∼ -1.8 eV correspond to d_{xy} and $d_{yz/zx}$ orbitals, respectively, and the parabolic band dispersion is derived from d_{xy} orbital. The orbital character revealed by the present study is consistent with the theoretical prediction [3].
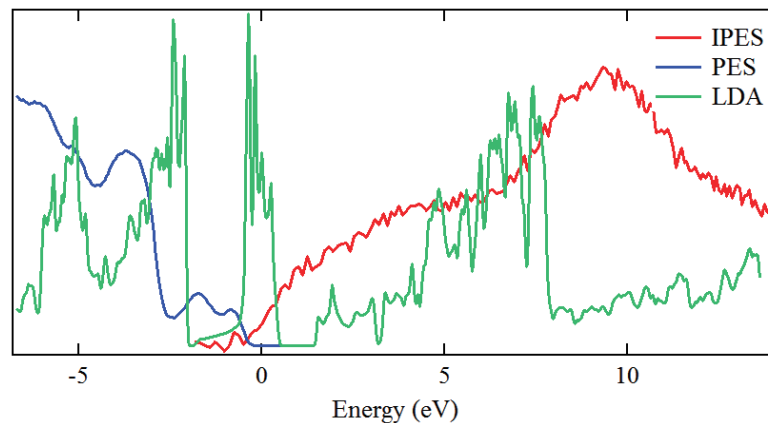
FIGURE 1. Compared with the LDA calculation (green), PES (blue) and IPES (red) spectrum of $Ca_{2-x}Sr_xRuO_4$ (x = 0.06) taken at $hv = 23$ eV and $E_k = 58$ eV, respectively.
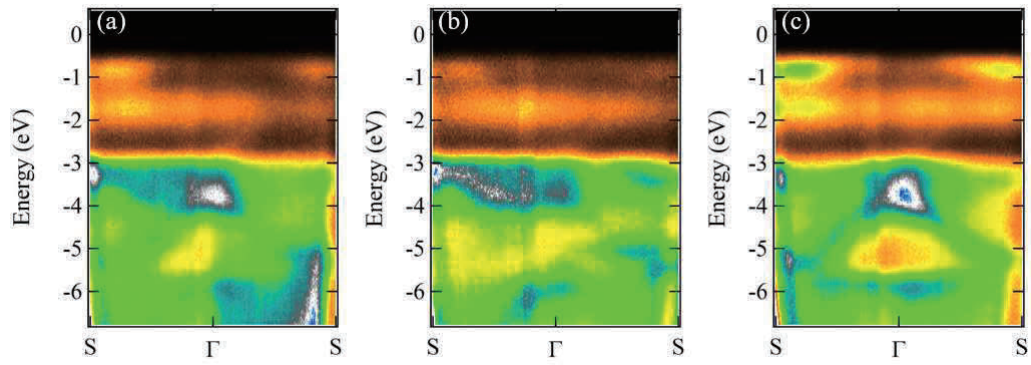
FIGURE 2. ARPES spectra of Ca$_{2-x}$Sr$_x$RuO$_4$ (x = 0.06) using (a) circular-polarized, (b) *p*-polarized and (c) *s*-polarized incident light at $h\nu$ = 23 eV.

REFERENCES

1. S. Nakatsuji and Y. Maeno, Phys. Rev. Lett. **84**, 2666 (2000).
2. S. Nakatsuji *et al*., Phys. Rev. Lett. **90**, 137202 (2003).
3. V. I. Anisimov *et al*., Eur. Phys. J. B, **25**, 191 (2002).

Angle-resolved Photoemission Spectroscopy Study on $Rb_xFe_{2-y}Se_2$ superconductor

M. Sunagawa[a], K. Terashima[a,b], H. Fujiwara[a], T. Fukura[a], A.Takeda[a],
M. Tanaka[c], H. Takeya[c], Y. Takano[c], M. Arita[d], K. Shimada[d], H. Namatame[d],
M. Taniguchi[d], K. Suzuki[e], H. Usui[f], K. Kuroki[f], T. Wakita[a,b], Y. Muraoka[a,b],
and T. Yokoya[a,b]

[a]The Graduate School of Natural Science and Technology and Research Laboratory for Surface
Science, Okayama University, Okayama 700-8530, Japan
[b]Research Institute for Interdisciplinary Science (RIIS), Okayama University, Okayama 700-
8530, Japan
[c]MANA, National Institute for Materials Science, 1-2-1 Sengen, Tsukuba, Ibaraki 305-0047,
Japan
[d]Hiroshima Synchrotron Radiation Center, Hiroshima University, Higashi-Hiroshima,
Hiroshima 739-0046, Japan
[e]Research Organization of Science and Technology, Ritsumeikan University, 1-1-1 Noji-higashi,
Kusatsu, Shiga 525-8577, Japan
[f]Department of Physics, Osaka University, 1-1 Machikaneyama, Toyonaka, Osaka 560-0043,
Japan.

Keywords: Iron-based superconductor, ARPES

In the study of iron-based superconductors, one of the ultimate goals is to clarify the common feature that produces the high critical temperature (T_c). Based on a weak-coupling viewpoint [1,2], spin and/or orbital fluctuation mediated superconductivity has been proposed for the mechanism of the superconductivity. In this theory, the Fermi surface (FS) nesting between hole-like FSs and electron-like FSs has been considered to be a key ingredient for the emergence of high T_c in iron-based superconductors. In fact, in iron-arsenide superconductors, the FS topology consisting of hole- and electron-like FSs has been commonly observed. Thus, coexistence of hole- and electron-like FSs was considered to be a common feature in high-T_c iron-based superconductors.

However, since ever the discovery of in alkali-metal-doped iron-selenide superconducotrs with $T_c = 32$ K, an understanding of common electronic structure for the emergence of high-T_c is yet to be achieved. Previous angle-resolved photoemission spectroscopy (ARPES) studies in alkali-metal-doped iron-selenide superconductors reported absence of the hole-like FS in this material [3,4]. Its high T_c and unique FS topology that consists of only the electron-like FSs pose a challenge on the theoretical description of high-T_c superconductivity based on the FS nesting scenario.

Recently, we reported ARPES measurements of the high-quality $K_{0.62}Fe_{1.7}Se_2$ single crystal [5], where a hidden hole-like band approaching the Fermi level (E_F) around the Γ point was observed, suggesting that a hole-like FS exists in $K_xFe_{2-y}Se_2$ [6]. This result indicates that the alkali-metal doped iron selenides, with both

electron- and hole-like FSs present, can be categorized in the same group as that of the iron arsenides. In order to confirm this indication, further experimental investigation is needed to clarify whether the hidden hole-like band commonly exists in alkali-metal doped iron selenides.

In this study, we performed ARPES measurements with careful tuning of photon energy and photon polarization on a high quality single crystal of $Rb_xFe_{2-y}Se_2$ prepared by the one-step synthesis [5], and we succeeded to observe the hidden hole-like band whose top almost touches E_F around the Z point, suggesting that a hole-like FS exists in $Rb_xFe_{2-y}Se_2$. The present study provides further experimental evidence to support the indication that the alkali-metal doped iron selenides and the iron arsenides can be categorized in the same group from the viewpoint of the FS topology. Thus, the common feature of the iron-based superconductors may be the presence of hole- and electron-like FSs.

REFERENCES

[1] I. I. Mazin *et al*., Phys. Rev. Lett. **101**, 057003 (2008).

[2] K. Kuroki *et al*., Phys. Rev. Lett. **101**, 087004 (2008).

[3] Y. Zhang *et al*., Nat. Mater. **10**, 273 (2011).

[4] T. Qian *et al*., Phys. Rev. Lett. **81**, 140508 (2012).

[5] M. Tanaka *et al.*, J. Phys. Soc. Jpn, **85**, 044710 (2016).

[6] M. Sunagawa *et al.*, J. Phys. Soc. Jpn, **85**, 073704 (2016).

Momentum dependence of the electronic structure in YbInCu$_4$ revealed by angle-resolved photoemission spectroscopy

S. Ishihara[a], K. Ichiki[a], K. Abe[a], T. Matsumoto[a], K. Mimura[a,b], H. Sato[b], M. Arita[b], H. Namatame[b], M. Taniguchi[b], T. Zhuang[c], K. Hiraoka[c], and H. Anzai[a]

a Graduate School of Engineering, Osaka Prefecture University, Sakai 599-8531, Japan
b Hiroshima Synchrotron Radiation Center (HSRC), Hiroshima University, Higashi-Hiroshima 739-0046, Japan
c Graduate School of Science and Engineering, Ehime University, Matsuyama 790-8577, Japan

In rare-earth compounds, the hybridization between conduction and localized-*f* electrons (*c-f* hybridization) has been one of the most intriguing subjects. In particular, YbInCu$_4$ has attracted great interests for a long time. YbInCu$_4$ exhibits a first-order valence transition at T_v = 42 K and concomitantly changes Kondo temperature, which is a measure of the *c-f* hybridization strength, from $T_K \sim$ 25 K in high-temperature phase to $T_K \sim$ 400 K in low-temperature phase [1,2]. Hence, the *c-f* hybridization is closely related to the valence transition.

Angle-resolved photoemission spectroscopy (ARPES) is a direct probe to measure the electronic excitation as functions of energy and momentum. Our recent ARPES study of YbInCu$_4$ revealed that the flat band at $|\omega| \sim$ 0.13 eV is derived from the Yb 4f state in the subsurface region that intervenes between the surface and bulk regions of crystal [3]. The flat band shows a momentum-dependent behavior around the $\overline{\text{M}}$ point of the two-dimensional Brillouin zone and its energy distribution is described well by the periodic Anderson model. To gain further insight into the *c-f* hybridization effect, we have performed high-resolution ARPES measurements of YbInCu$_4$ and determined the band structure in a wide momentum space. We show the presence of a large hybridization gap at the $\overline{\Gamma}$ point.

Single crystals of YbInCu$_4$ with C15b-type structure were grown by the flux method with InCu$_2$ flux. The ARPES measurements were performed at BL-9A of Hiroshima Synchrotron Radiation Center. Total energy resolution was set to 20 meV. The samples were cleaved *in situ* along the (111) crystal plane. All the data were collected at 8 K in a vacuum better than 2.6×10^{-10} Torr. The excitation photon energy was $h\nu$ = 24 eV.

Figure 1(b) and 1(e) show photoemission intensity plot, $I(k,\omega)$, along cut #1 and #2 marked in Fig. 1(a), respectively. For a better view of the band dispersions, we also plot the corresponding second derivative of the photoemission intensity with respect to the energy, $\partial^2 I(k,\omega)/\partial\omega^2$, in Figs. 1(c) and 1(f). An intense flat band is visible clearly at $|\omega| \sim$ 0.05 eV and is assigned to the bulk-derived Yb^{+2} 4$f_{7/2}$ state [4].

Along cut #1, a flat band at $|\omega| \sim$ 0.13 eV below the bulk Yb^{+2} 4$f_{7/2}$ state becomes a parabolic electronlike band around $|k| <$ 0.15 Å^{-1}, as shown in energy distribution curves (EDCs) of Fig. 1(d). The bottom of the band is estimated to be ~0.20 eV. This momentum-dependent behavior near the $\overline{\text{M}}$ point is consistent with our previous study, concerning the hexagonal symmetry of the lattice [4]. The 0.13 eV flat band is thus assigned to the Yb 4f states derived from the Yb atom in subsurface region of the YbInCu$_4$ crystals [4,5]. It can be seen that this band is pushed smoothly downward in energy at $k \sim$ 0 Å^{-1}.

Along cut #2, on the other hand, the flat band splits into two components: one branch is shifted downward in energy to ~0.22 eV, and the other is shifted upward in energy to ~0.10 eV, as shown in Figs. 1(f) and 1(g). Similar energy splitting in 4f-derived bands has been observed in EuNi$_2$P$_2$ and assigned to the hybridization phenomena [6]. This similarity suggests the hybridization effect between the 4f-derived state at 0.13 eV and itinerant electrons. The energy separation at the $\overline{\Gamma}$ point is estimated to be 0.12 eV. Our results indicate the momentum-dependent hybridization effect between the conduction and 4f electrons in the subsurface region of YbInCu$_4$.
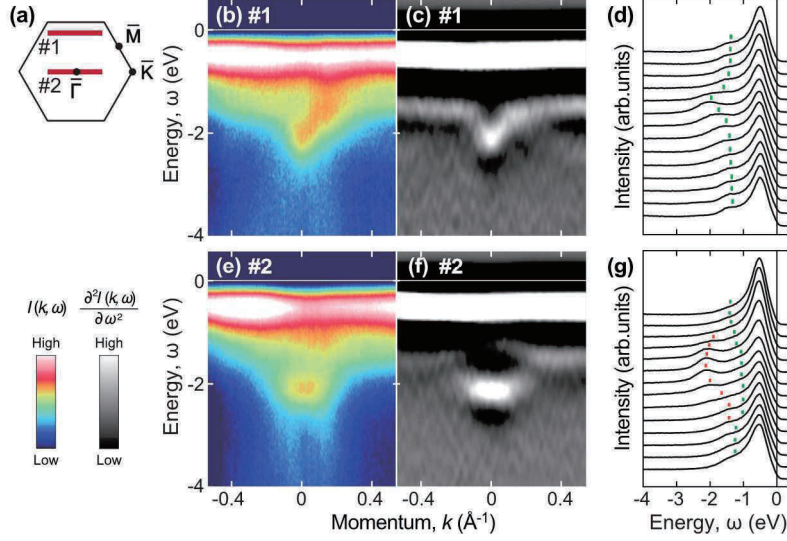
Figure 1. (a) The two-dimensional Brillouin zone of YbInCu$_4$. (b), (e) Photoemission intensity plot $I(k,\omega)$ taken along cut #1 and #2 marked in (a), respectively. (c), (d) The corresponding second derivative of the photoemission intensity $\partial^2 I(k,\omega)/\partial\omega^2$ of (b) and (e), respectively. (d), (g) The energy distribution curves for the data in (b) and (e), respectively. The vertical bars indicate the peak positions. All the data were collected at $T = 8$ K with $h\nu = 24$ eV.

In summary, we report ARPES studies on the first-order valence-transition compound YbInCu$_4$ in the low-temperature phase. The opening of the hybridization gaps is observed clearly in the subsurface band around the $\bar{\Gamma}$ point. The energy separation at $k \sim 0$ Å^{-1} is ~0.12 eV. Our results imply that the momentum-dependent hybridization effect between the conduction and $4f$ electrons in the subsurface region is relevant to the valence transition phenomena of YbInCu$_4$.

REFERENCES

1. I. Felner *et al.*, Phys. Rev. B **35**, 6956 (1987).
2. J. L. Sarrao, C. D. Immer, C. L. Benton, and Z. Fisk, Phy. Rev. B **54**, 12208 (1996).
3. S. Ishihara *et al.*, J. Electron Spectrosc. Relat. (2016).
4. F. Reinert *et al.*, Phys. Rev. B **58**, 12808 (1998).
5. S. Suga *et al.*, J. Phys. Soc. Jpn. **78**, 074704 (2009).
6. S. Danzenbächer *et al.*, Phys. Rev. Lett. **102**, 026403 (2009).

Temperature-dependent Angle-resolved Photoemission Spectroscopy Study on $K_xFe_{2-y}Se_2$ superconductor

M. Sunagawa[a], K. Terashima[a,b], H. Fujiwara[a], T. Fukura[a], A.Takeda[a],
M. Tanaka[c], H. Takeya[c], Y. Takano[c], M. Arita[d], K. Shimada[d], H. Namatame[d],
M. Taniguchi[d], K. Suzuki[e], H. Usui[f], K. Kuroki[f], T. Wakita[a,b], Y. Muraoka[a,b],
and T. Yokoya[a,b]

[a]The Graduate School of Natural Science and Technology and Research Laboratory for Surface Science, Okayama University, Okayama 700-8530, Japan
[b]Research Institute for Interdisciplinary Science (RIIS), Okayama University, Okayama 700-8530, Japan
[c]MANA, National Institute for Materials Science, 1-2-1 Sengen, Tsukuba, Ibaraki 305-0047, Japan
[d]Hiroshima Synchrotron Radiation Center, Hiroshima University, Higashi-Hiroshima, Hiroshima 739-0046, Japan
[e]Research Organization of Science and Technology, Ritsumeikan University, 1-1-1 Noji-higashi, Kusatsu, Shiga 525-8577, Japan
[f]Department of Physics, Osaka University, 1-1 Machikaneyama, Toyonaka, Osaka 560-0043, Japan.

Keywords: Iron-based superconductor, ARPES

Among iron-based superconductors, $A_xFe_{2-y}Se_2$ (superconducting transition temperature; $T_c \sim 32$ K [1]) is a unique system because it exhibits intrinsic phase separation, leading a coexistence of several phases. So far, the coexisting two phases with different electronic property are well known in $A_xFe_{2-y}Se_2$ [2]. One phase, so-called 245 phase, is insulating with a stoichiometry of $A_{0.8}Fe_{1.6}Se_2$ with $\sqrt{5} \times \sqrt{5}$ ordered Fe vacancy. Another phase, so-called 122 phase, is metallic with a stoichiometry of $A_xFe_{2-\delta}Se_2$ with disordered Fe vacancy. Based on the previous ARPES studies, it is widely believed that the near-E_F electronic state (-400 meV $< E - E_F < 0$ meV) would be derived from only the 122 phase [3]. Temperature-dependent ARPES studies on $K_xFe_{2-y}Se_2$ have reported the development of incoherent behavior for the specific bands in the near-E_F band structure at higher temperature [4]. In order to explain this result, the orbital selective Mott transition in the 122 phase has been proposed. In this model, above the transition temperature, only the d_{xy} orbital is the insulating state, and the other orbitals remain metallic state.

However, recent our ARPES study on $K_xFe_{2-y}Se_2$ has revealed that the number of the observed bands around the Brillouin zone center (Γ point) near E_F is larger than the band calculation [5]. This suggests that the near-E_F electronic structure cannot be explained by only the 122 phase. In order to confirm this implication, it is important to clarify whether the orbital selective Mott transition in the 122 phase can explain the temperature dependence of all the observed bands.

In this study we performed temperature-dependent ARPES measurement of the high-quality $K_{0.62}Fe_{1.7}Se_2$ single crystal [6] to reveal the evolution of band structure as a function of temperature. At $T = 40$ K, we newly discovered the existence of three electron-like bands at the Brillouin zone corner (M point), demonstrating that the number of the observed bands at both the Γ and the M points is also larger than the band calculation. In addition, we found that two bands at the Γ point and one band at the M point show strong suppression of intensity with increasing the temperature. This result cannot be explained completely by the orbital selective Mott transition, where only the band with d_{xy} character disappeared at the Γ point and the M point, respectively. These results clearly show that the near-E_F band structure in $K_xFe_{2-y}Se_2$ cannot be fully explained by one metallic phase. Compared to the recent high-energy x-ray emission and absorption studies [7,8], we speculate that the observed bands are derived from both the 122 phase and the interface phase that exists at the interface between 122 phase and 245 phase.

REFERENCE

[1] J. Guo *et al.*, Phys. Rev. B **82**, 180520 (2010).

[2] A. Ricci *et al*, Phys. Rev. B **84**, 060511 (2011).

[3] F. Chen *et al,* Phys. Rev. X **1**, 021020 (2011).

[4] M. Yi *et al*., Phys. Rev. Lett. **110**, 067003 (2013).

[5] M. Sunagawa *et al.*, J. Phys. Soc. Jpn, **85**, 073704 (2016).

[6] M. Tanaka *et al.*, J. Phys. Soc. Jpn, **85**, 044710 (2016).

[7] A. Ricci *et al.,* Phys. Rev. B **91**, 020503 (2015).

[8] L. Simonelli *et al*., Phys. Rev. B **90**, 214516 (2014).

Spin-resolved electronic band structure
of a metallic TMDC: 3R-NbS$_2$

Ch. Datzer[a], P. Eickholt[a], K. Miyamoto[a,b], T. Okuda[b], and M. Donath[a]

[a]*Physikalisches Institut, Westfälische Wilhelms-Universität Münster,*
Wilhelm-Klemm-Straße 10, 48149 Münster, Germany
[b]*Hiroshima Synchrotron Radiation Center, Hiroshima University,*
*2-313 Kagamiyama, Higashi-Hiroshima 739-0046, Japan*

Keywords: Spin-resolved ARPES, electronic band structure, TMDC, NbS$_2$

The discovery of graphene triggered a pursuit in research on two-dimensional (2D) materials [1]. Beside materials such as boron nitride, transition metal dichalcogenides (TMDCs) have recently attracted remarkable interest. Interesting optical properties combined with spin-polarized electronic valleys make them promising materials for future applications in opto-, valley- and spintronics [2–7].

One member of the TMDC family is the metallic NbS$_2$. For novel devices, using heterostructures, NbS$_2$ is a promising candidate as buffer material between the metal contact and 2D materials such as graphene, hBN and semiconducting TMDCs [8-10]. It is also known as possible material for Li batteries [11-12] due to its layered structure opening the way for intercalation.

NbS$_2$ crystallizes in two different structures: 2H$_a$ (inversion symmetric) and 3R. Interesting for spintronic applications is the non-centrosymmetric 3R structure with presumably interesting spin textures for the entire crystal [7].

So far, no experimental information about the electronic band structure and spin texture of NbS$_2$ is reported. Here, we present a spin-resolved ARPES study on 3R-NbS$_2$.
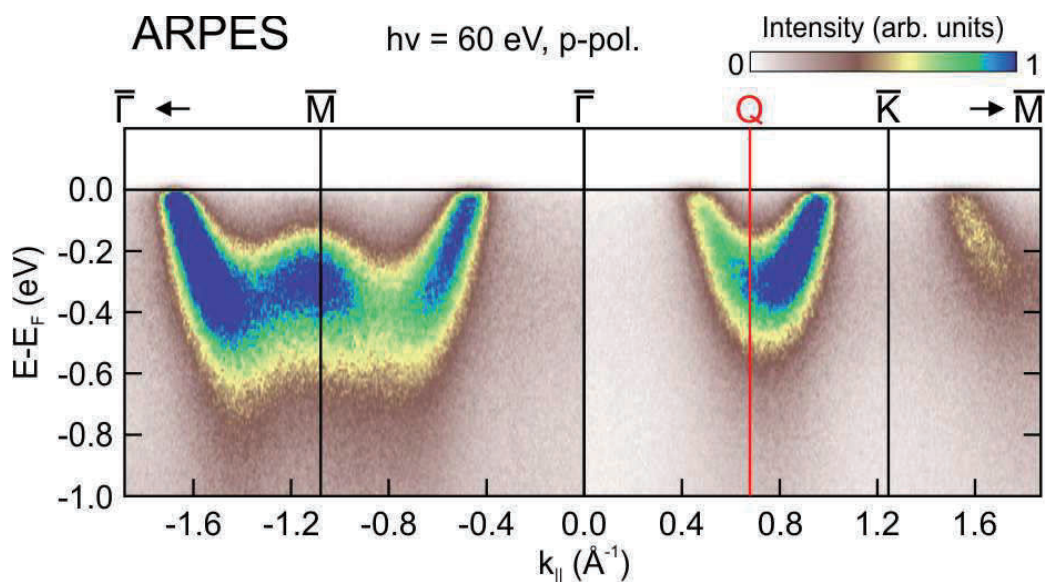
FIGURE 1. ARPES experiment (hv = 60 eV) within 1 eV below the Fermi edge along high-symmetry directions of the surface. Q marks the $k_{\parallel}$ value, where the spin-resolved data of Fig. 2 have been obtained.

The experimental ARPES results for hv = 60 eV are displayed in Fig.1 as a contour plot. The photoelectron intensity is shown as a function of the energy referred to the Fermi level E_F and the momentum $k_\parallel$ along high-symmetry directions of the surface Brillouin zone. Around the M point, a "W"-like feature is observed, while, in the ΓK direction, a "V"-like valley structure is detected. Due to the non-centrosymmetric crystal structure and its C_{3v} symmetry, a non-zero out-of-plane spin polarization along ΓK is expected. Figure 2 displays the spin-resolved ARPES results for the out-of-plane spin polarization P_z. The data is obtained within the valley-like structure at $k_\parallel$ = Q between the Γ and the K points.
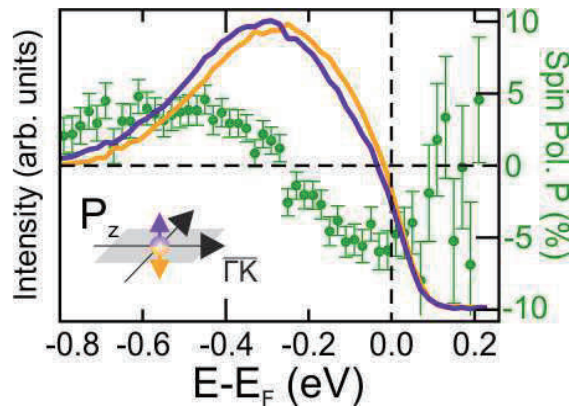
FIGURE 2. Results of a spin-resolved ARPES experiment (hv = 60 eV) at $k_\parallel$ = Q between Γ and K, as defined in Fig. 1.

The data shows a spin-polarization component in z direction of up to 6%. A distinct spin splitting of the bands within the Q valley is observed, which amounts to about 50 meV. Further comprehensive spin-resolved measurements along ΓK with various photon energies are needed to reveal the intrinsic 3D spin texture and its value for novel applications.

REFERENCES

1. A. K. Geim and K. S. Novoselov, *Nature Mateirals* **6**, 183 (2007).
2. K. Mak *et al.*, *Physical Review Letters* **105**, 136805 (2010).
3. K. Mak *et al.*, *Nature Nanotechnology* **7**, 494 (2012).
4. Z. Gong *et al.*, *Nature Communications* **4**, 2053 (2013).
5. A. M. Jones *et al.*, *Nature Physics* **10**, 130 (2014).
6. Y. Y. Zhang *et al.*, *Science* **344**, 725 (2014).
7. R. Suzuki *et al.*, *Nature Nanotechnology* **9**, 611 (2014).
8. M. Farmanbar *et al.*, *Advanced Electronic Materials* **2**, 1500405 (2016).
9. Y. Liu *et al.*, *Science Advances* **2**, e1600069 (2016).
10. C. Zhang *et al.*, *2D Materials* **4**, 015026 (2017).
11. J. Molenda *et al.*, *Physica Status Solidi* **156**, 159 (1996).
12. Y. Liao *et al.*, *Journal of Power Sources* **245**, 27 (2014).

Spin-resolved ARPES of a Kondo insulator YbB$_{12}$

K. Hagiwara[a], Y. Ohtsubo[b,a], J. Kishi[a], M. Matsunami[c], S. Ideta[c], K. Tanaka[c],

H. Miyazaki[c] J. E. Rault[d], P. Le Fèvre[d], F, Bertran[d], A. Taleb-Ibrahimi[d,e],

R. Yukawa[f], M. Kobayashi[f], K. Horiba[f], H. Kumigashira[f], K. Sumida[g],

T. Okuda[h], F. Iga[i], S. Kimura[b,a],

[a]*Department of Physics, Graduate School of Science, Osaka University, Toyonaka 560-0043, Japan.*
[b]*Graduate School of Frontier Biosciences, Osaka University, Suita 565-0871, Japan.*
[c]*UVSOR Facility, Institute for Molecular Science, Okazaki 444-8585, Japan.*
[d]*Synchrotron SOLEIL, Saint-Aubin-BP 48,F-91192 Gif sur Yvette, France.*
[e]*UR1/CNRS-Synchrotron SOLEIL, Saint-Aubin, F-91192 Gif sur Yvette, France.*
[f]*Photon Factory, Institute of Materials Structure Science, High Energy Accelerator Research Organization (KEK), 1-1 Oho, Tsukuba 305-0801, Japan.*
[g]*Graduate School of Science, Hiroshima University,1-3-1 Kagamiyama, Higashi-Hiroshima 739-8526, Japan.*
[h]*HiSOR, Hiroshima University, Higashi-Hiroshima 739-0046, Japan.*
[i]*College of Science, Ibaraki University, Mito 310-8512, Japan.*

Ytterbium dodecaboride YbB$_{12}$ is one of Kondo insulators/semiconductors (KIs), which has a tiny energy gap owing to the hybridization between conduction and localized $4f$ electrons, namely c-f hybridization [1]. Although the bulk energy gap is fully opened [2], the electrical resistivity is saturated at lower temperature than 10 K. The origin of the saturation is expected to be a topologically protected metallic surface state, namely "topological Kondo insulator" (TKI) [3]. Spin polarization structure identical to TKI is theoretically expected, however that has not been reported. So this time, to elucidate the origin of the metallic conduction at the surface, we performed the ARPES and Spin-resolved ARPES (SARPES) of a well-defined surface of YbB$_{12}$.

Figure 1 shows ARPES and SARPES results near the Fermi level. Figure 1 (a) is the intensity map at E$_F$ obtained by ARPES measurement taken at 15K with the excitation photon energy of 53.5 eV. The image shows metallic conduction band and that state forms closed Fermi surface surrounding highly symmetry point. Figure 1 (b)-(e) shows spin-resolved ARPES results (at k$_{//}$ ~ ± 0.2 Å^{-1} in Fig. 1) taken at 20 K with photon energy 53.5 eV. Clear spin polarization indicating helical spin structure was observed and it is consistent with the behavior expected as topological surface state near the Fermi level.

These characters of band dispersion obtained by ARPES and SARPES measurements, such as metallic at low temperature, helical spin polarization near Fermi level is well consistent with the expected behavior for surface state on TKIs [4].
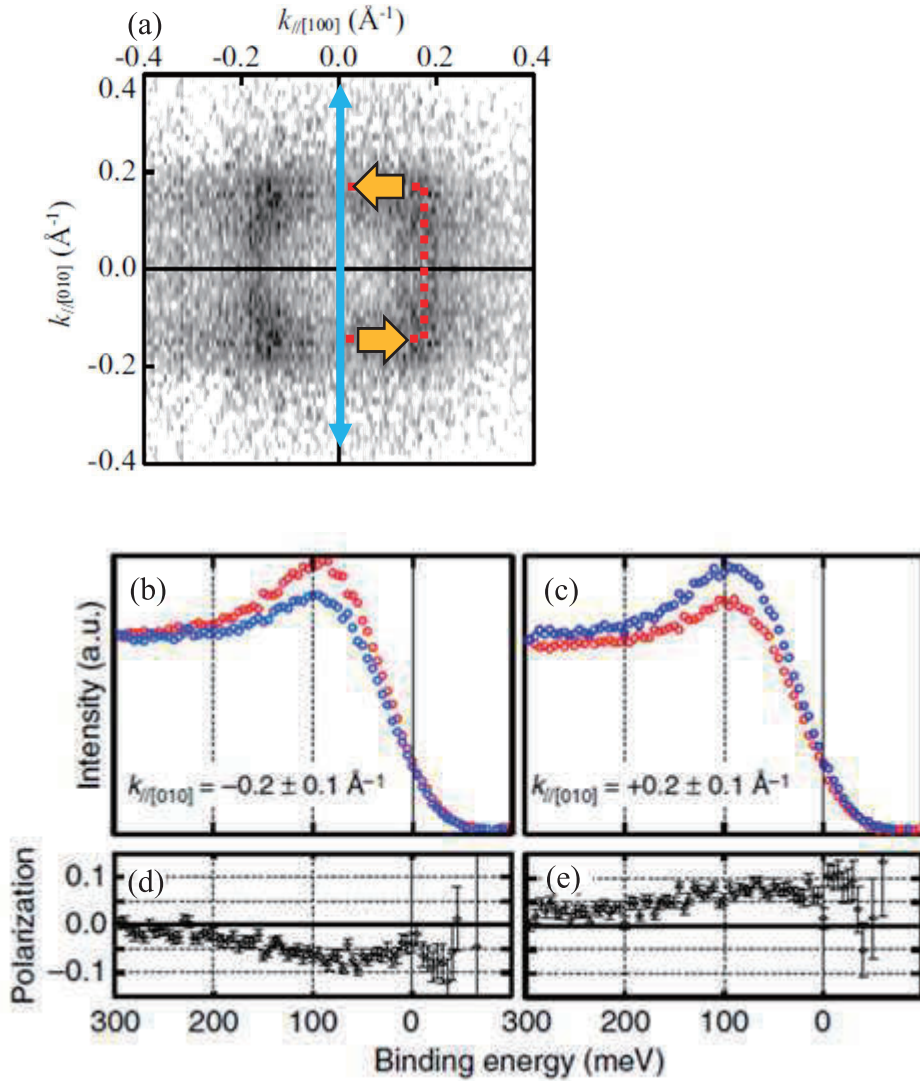
Fig.1 ARPES and SARPES image of YbB$_{12}$ near Fermi energy.

(a) Constant energy contour obtained by ARPES measurement taken at 15K with photon energy 53.5 eV.
Red lines are guides for eye, and blue and yellow arrows correspond to the measuring direction and spin direction (obtained by (b)-(e) spin texture.), respectively.
(b, c)Spin-resolved ARPES energy distribution curves (EDC) taken at 20 K. Blue (red) spectra corresponds with the spin direction parallel (anti-parallel) to [100]. (c, d) Spin polarizations of the EDC shown in (a, b), respectively. Positive (negative) value represents the spin polarization parallel (anti-parallel) to [100]. Errors are standard statistical errors from photoelectron counting.

REFERENCES

1. F. Iga *et al*., JMMM **177–181**, 337 (1998).
2. H. Okamura *et al*., JPSJ **74**, 1954 (2005).
3. M. Dzero *et al*., PRL **104**, 106408 (2010).
4. K. Hagiwara *et al*., Nat. Commun. **7,** 12690 (2016).

Direct evidence of hidden local spin polarization in novel superconductor $LaO_{0.55}F_{0.45}BiS_2$

S. Wu[A], K. Sumida[B], K. Miyamoto[A], K. Taguchi[B], T. Yoshikawa[B], A. Kimura[B], Y. Ueda[A], M. Nagao[C], S. Watauchi[C], I. Tanaka[C], and T. Okuda[A]

[A]Hiroshima Synchrotron Radiation Center (HSRC), Hiroshima University,

[B]Graduate School of Science, Hiroshima University,

[C]Center for Crystal Science and Technology (CCST), Yamanashi University

Keywords: spin-ARPES, Rashba-Dreselhaus effect, spin polarization, super conductor

Conventional Rashba spin polarization is caused by the combination of strong spin-orbit interaction (SOI) and spatial inversion asymmetry. However, Rashba- and Dresselhaus-type spin split states are predicted in $LaOBiS_2$ system by recent theory even though the total crystal structure is centrosymmetric, stemming from local inversion asymmetry of each active BiS_2 sublayer [1] of the system. By performing high-resolution spin-ARPES measurement at ESPRESSO endstation of Hiroshima Synchrotron Radiation Center (HiSOR), we have obtained direct spectroscopic evidence for the local spin polarization in the vicinity of X point of both valence band and conduction band. Especially the transition from Rashba-like to Dresselhaus-like spin texture has been observed in the conduction band for the first time.

As shown in Fig. 1(a), the conduction band splits into inner and outer branches along k_x direction. Fig. 1(b) shows unambiguously spin polarized states at the momenta labeled as "1" to "4" and spin polarizations at the positions "1" and "2" are opposite to those of positions "3" and "4" in the spin-resolved EDCs spectra such that the spin reversal can be observed on opposite sides of "X" point where is a time-reversal invariant momenta (TRIM). Similarly, we also performed spin-ARPES measurement along k_y direction and observed spin reversal at two sides of "X" momenta again. Especially we found that the spin polarization near the X point is also opposite to that of at the momentum position further from the X point indicating the transition from Dresselhaus-like to Rashba-like spin texture. The change of spin texture with varying binding energy in the conduction band is considered as a consequence of mixing of local Rashba-Dresselhaus effect. In addition, the spin-ARPES results of highest valence band (HVB) also shows local spin polarization (not shown here). Our studies present direct evidence for the existence of local Rashba and Dresselhaus spin polarizations around TRIM X point in novel BiS_2 based superconductor. The demonstration not only expands the range of spintronic materials but also serves as a new platform for research of superconductivity caused by spin-split conduction band [2].
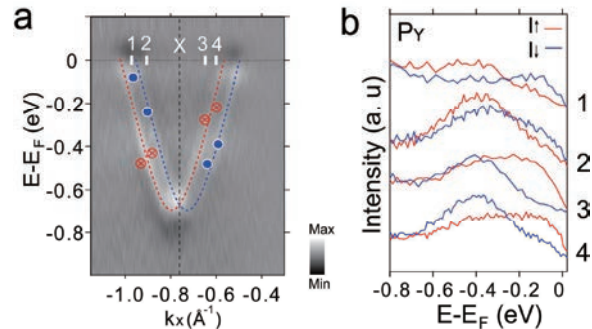

Fig. 1 (a) Conduction band dispersion around X point (second derivative). "1" to "4" represent the momenta where we performed spin-ARPES measurement. (b) Spin-resolved EDCs at "1" to "4" momenta.

References

[1] Zhang, X. et al. *Nat Phys*. **10**, 387-393 (2014).

[2] Yang, Y. et al. *Phys Rev B*. **88**. 094519 (2013).

Unusual Spin Texture in "Minimum Weyl" Material TaIrTe$_4$

S. V. Borisenko[a], E. Haubold[a], Y.Kushnirenko[a], K. Sumida[b], K. Taguchi[b], T. Yoshikawa[b], A. Kimura[b], T. Okuda[c]

[a]IFW Dresden, Helmholtzstr. 20, 01069 Dresden, Germany
[b] School of Science, Hiroshima University, 1-3-1 Kagamiyama, Higashi-Hiroshima 739-8526, Japan
[c] Hiroshima Synchrotron Radiation Center (HSRC), Hiroshima University, 2-313 Kagamiyama, Higashi-Hiroshima 739-0046, Japan

We present experimental evidence for type-II non-centrosymmetric Weyl state in TaIrTe$_4$ where it has been recently predicted theoretically [1]. In particular, we observe the exotic surface states, which support the quasi-1D Fermi arcs connecting only four Weyl points (WP). These electronic states are spin-polarized in the direction along the arcs, thus highlighting TaIrTe$_4$ as a novel type-II Weyl semimetal with promising application potential.

The details of the electronic structure of this material have been clarified by some of the authors earlier [2] and the beamtime at HiSOR has been devoted, in particular, to the determination of the spin character of the unique surface states. According to the calculated spectral function (see and Fig. 3 in Ref. 2), these surface states in the case of (001) surface are located at the edge of the large hole-like Fermi surface (FS).

In panels (a) and (d) of Fig. 1 we show theoretical calculated data for the cuts through the Fermi arc for two positions with $k_y < k_y$(WP) (a) and for $k_y > k_y$(WP) (d), comparing them with two experimental cuts in momentum space which cross the FS arcs, shown in panels (b, c, e, f). One can identify the topological surface states as sharpening of the intensity on the inner sides of the smeared out intensity corresponding to 3D dispersions of the hole-pockets. This is confirmed by the maxima in MDCs (white solid lines in panels (b) and (e)) and by the second-derivative plots in panels (c) and (f). The agreement with the calculations is both qualitative and quantitative, as the Fermi velocity is ~1 eV Å in all cases.

In Fig. 1 (g) we show the second derivative of the FS map, where the Fermi arcs are seen directly and with unprecedented clarity. Also the shape of the arcs strongly resembles the calculated ones seen at the borders of large hole-pockets. As is predicted theoretically and shown experimentally for (001) surface, the arcs in TaIrTe$_4$ are peculiar: they are long and reasonably straight. With these characteristics in mind one would obviously be interested to learn about the spin of these states from the point of view of applications in spintronics.

In Fig. 1 (h-o) we present the spin-resolved measurements from both surfaces of TaIrTe$_4$ collected at HiSOR Beamline 9B. We have analyzed the energy distribution curves which correspond to the topological surface states in different parts of the BZ. Because of the integration over a larger portion of the k-space for spin-resolved measurements the signal contains a contribution from the bulk states. Nevertheless, this contribution is significantly smaller than that collected from the surface state dispersion. There is always a clear signal corresponding to a particular direction of spin. The positive (negative) spin-polarization of a particular portion of the arc is given by red (blue) arrows while absence of spin-polarization is indicated by grey arrows. As it follows from Fig. 1 (h-j) for surface (001) and from Fig. 1 (k-o) for surface (00-1), the spins are always directed along the arcs and their directions are naturally opposite when k_y is inverted. We summarize our observations schematically in panel (k) in the lower part of Fig. 1. This spin texture is to be compared with the one of the Dirac states on the surfaces of the topological insulators. There the spins are directed tangentially to the circle Fermi surface. Due to spin-momentum locking, such arrangement is free from back scattering. In the case of TaIrTe$_4$ we have completely different topology of the spin directions: the spin-texture of arcs in TaIrTe$_4$ is strongly unidirectional implying a very anisotropic spin transport properties and even a possibility of storing the information. Indeed, both surfaces are characterized by the states with opposite spin separated in momentum space. Taking into account the strong anisotropy of the chiral anomaly expected in type-II Weyl semimetal, the experiments in magnetic and electric fields are urgently called for.
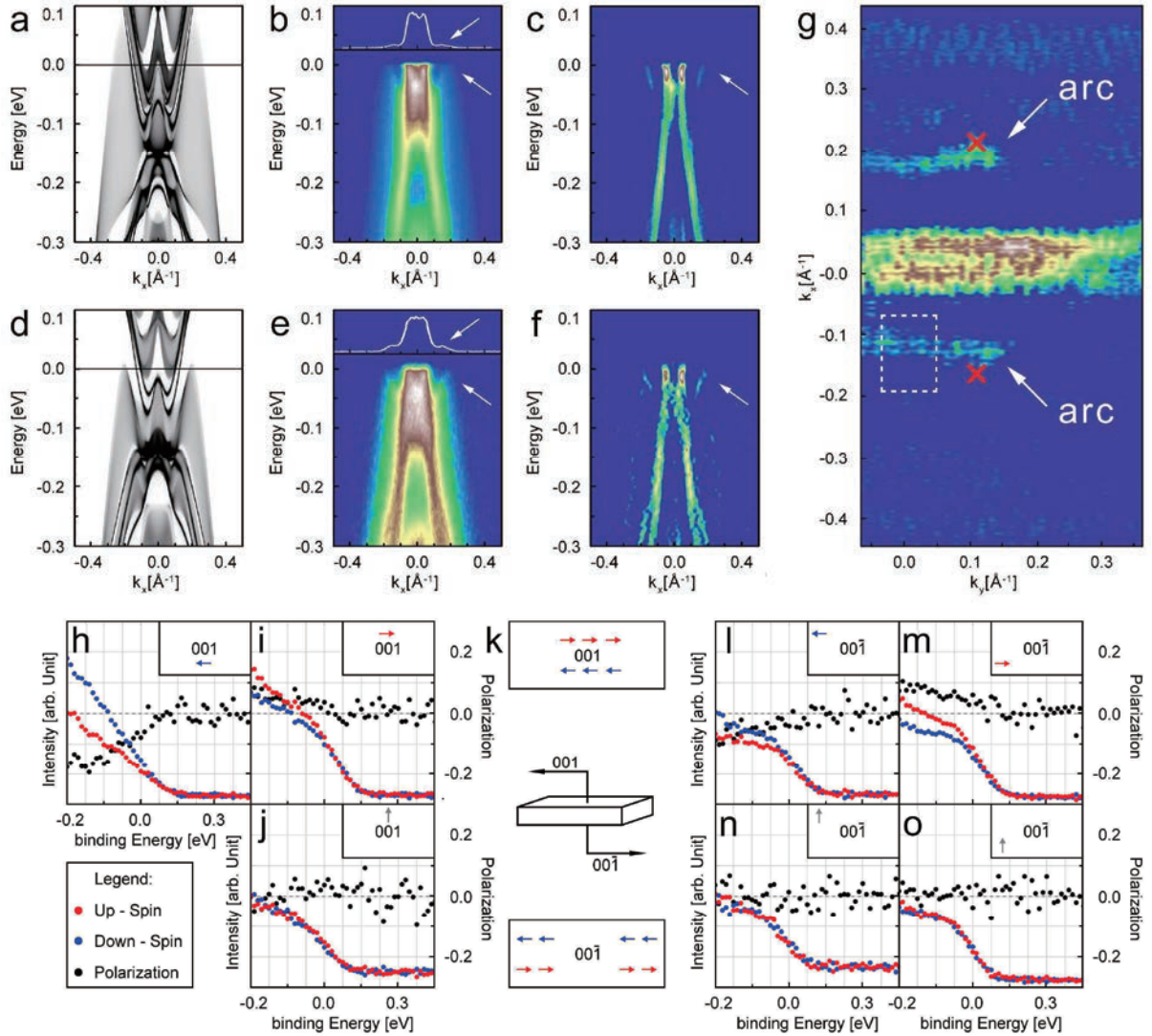
FIGURE 1. (From Ref. 2) (a) Spectral function of TaIrTe$_4$ calculated for $k_y = 0.05$ Å^{-1} and (d) for $k_y = 0.16$ Å^{-1}. (b, e) Corresponding ARPES data. Peaks in MDCs and dispersing features are shown by white arrows. (c, f) Second derivatives of the panels (b) and (e) highlighting the presence of the topological surface states. (g) Second derivative of the Fermi surface map of the second BZ. Arcs are clearly seen and are shown by the arrows. Weyl points are shown as red crosses and the positions of both cuts from (a-f) are indicated with dashed arrows. (h-j, l-o) Spin-resolved ARPES measurements performed at the points of the k-space schematically indicated by arrows next to the surface vector in the insets. (k) Schematically summary of the SARPES results. The electronic states on the arcs are spin-polarized as shown by the arrows within the BZ boundaries.

TaIrTe$_4$ thus emerges as a very interesting, from both fundamental and practical points of view, material. Although the Weyl points themselves lie above the Fermi level, the topological surface states which support the Fermi surface arcs are clearly present and reveal a unique spin-texture.

REFERENCES

1. K. Koepernik et al. "*TaIrTe₄: A ternary type-II Weyl semimetal*". Physical Review B93, p. 201101. doi:46310.1103/physrevb.93.201101.
2. E. Haubold, K. Koepernik, D. Efremov, S. Khim, A. Fedorov, Y.Kushnirenko, J. van den Brink, S. Wurmehl, B. Buchner, T. K. Kim, M. Hoesch, K. Sumida, K. Taguchi, T. Yoshikawa, A. Kimura, T. Okuda and S. V. Borisenko, Physical Review B, Rapid Communications (in press). arXiv:1609.09549.

Direct observation of spin-layer locking by local Rashba effect in monolayer PtSe₂ film

Wei Yao[1], Eryin Wang[1], Huaqing Huang[1], Ke Deng[1], Mingzhe Yan[1], Kenan Zhang[1], Koji Miyamoto[3], Taichi Okuda[3], Chaoxing Liu[4], Wenhui Duan[1,2] Shuyun Zhou[1,2]

1.   State Key Laboratory of Low-Dimensional Quantum Physics and Department of Physics, Tsinghua University, Beijing 100084, China
2.   Collaborative Innovation Center of Quantum Matter, Beijing 100084, China
3.   Hiroshima Synchrotron Radiation Center, Hiroshima University, Kagamiyama 2-313, Higashi-Hiroshima 739-0046, Japan
4.   Department of Physics, The Pennsylvania State University, University Park, State College, Pennsylvania 16802-6300, USA.

It has been recently suggested that spin polarization originates fundamentally from local atomic site asymmetries and therefore centrosymmetric materials may exhibit previously overlooked spin polarizations [1]. Here, by using spin- and angle-resolved photoemission spectroscopy, we report the observation of helical spin texture in monolayer, centrosymmetric and semiconducting PtSe₂ film without the characteristic spin splitting in conventional Rashba effect (R-1). First-principles calculations and effective analytical model analysis suggest local dipole induced Rashba effect (R-2) with spin-layer locking: opposite spins are degenerate in energy, while spatially separated in the top and bottom Se layers.
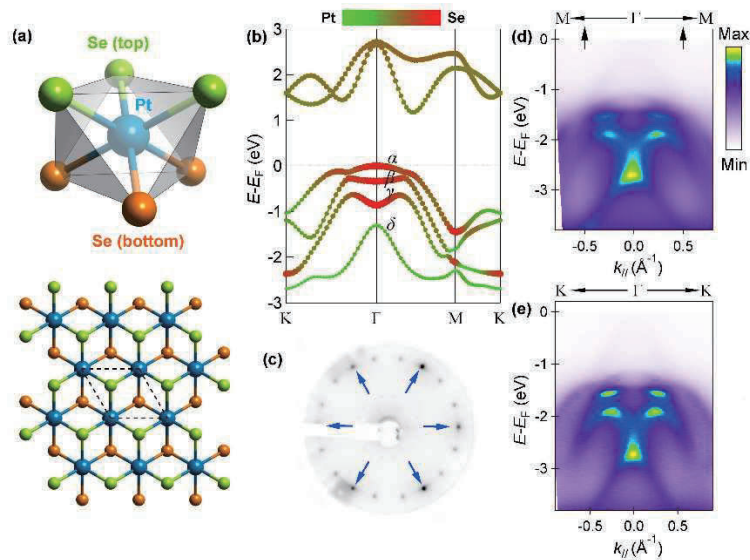
FIGURE 1: (a) Atomic structure of monolayer PtSe₂. (b) Calculated band structure of monolayer PtSe₂. (c) LEED pattern for the as-grown sample. (d) ARPES spectrum along G-M direction. (e) ARPES spectrum along G-K direction.

By utilizing direct selenization of a platinum substrate, we have successfully grown monolayer $PtSe_2$ thin film on the Pt substrate [2] with 1T structure (Fig. 1a). Figure 1b shows the calculated band structure. As monolayer $PtSe_2$ has both inversion and time-reversal symmetries, all these bands are expected to be doubly degenerate without any net spin polarization. Figure 1c shows the low-energy electron diffraction pattern of the high-quality sample. ARPES data measured along two high-symmetry directions M-G-M (Fig. 1d) and K-G-K (Fig. 1e), both show four valence bands with similar dispersions. The measured dispersions agree well with calculations except a shift in energy due to small charge transfer. Thus it suggests that the sample measured here can be approximated as quasi-freestanding monolayer $PtSe_2$.
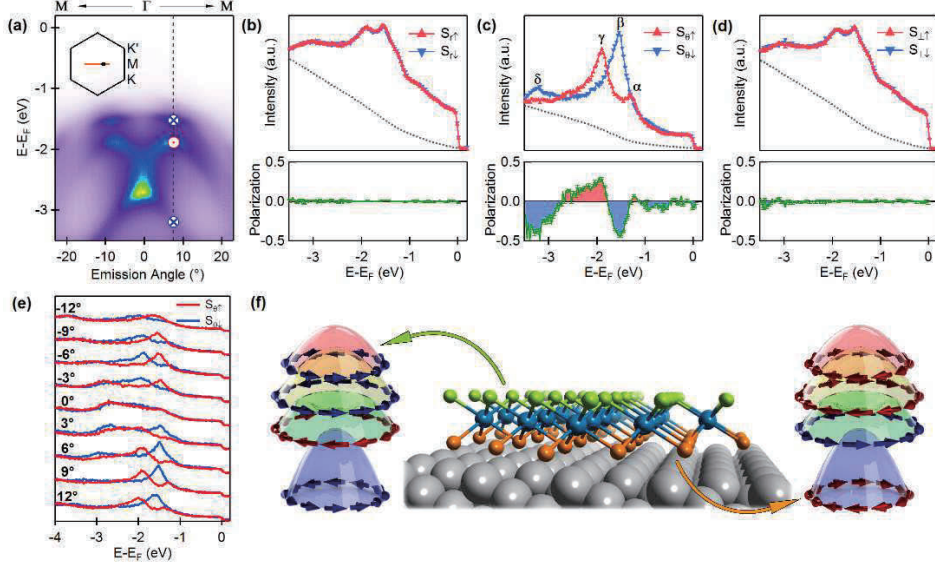
FIGURE 2: *(a) Measured dispersions along G-M direction. The dashed line indicates the position where the spin-resolved EDCs (b-d) are taken. (b-d) Spin-resolved EDCs for radial, tangent and out-of-plane components respectively. (e) Spin-resolved EDCs at different emission angles. (f) Schematic drawing for local Rahsba effect and spin-layer locking.*

Using the spin-resolved ARPES system at BL9B of HiSOR, we investigate the spin texture of $PtSe_2$ thin film. Figure 2 shows the results along G-M direction. Figure 2(b-d) are the spin-resolved EDCs for three spin components (radial, tangent and out-of-plane). It is clear that the tangent component has large spin polarization for the four valence bands, while the other two have negligible spin contrast. Moreover, the spin-resolved EDCs for tangent component at different emission angles (Fig. 2e) show that the spin polarization reverses on the other side of G point, demonstrating the time-reversal symmetry. Similar spin polarizations are also observed along the G-K direction. All these observations suggest a helical spin texture. Using first-principle calculations and effective model, we find that the experimental results can be explained by the loacal Rashba (R-2) effect, where a dipole field induces the observed spin polarization and leads to spin-layer locking (Fig. 2f).

In summary, we observe a large spin polarization in a semiconducting centrosymmetric 1ML $PtSe_2$. This provides the first experimental realization of spin-layer locking induced by local Rashba effect.

REFERENCE

1. Xiuwen Zhang *et al*. *Nature Physics,* **10**, 387–393 (2014)

2. Yeliang Wang *et al*. *Nano Lett.*, **15**, 4013–4018 (2015)

3. Wei Yao *et al*. *Nature Communication*, **8**, 14216 (2017)

Spin-Polarized Surface States at the Fermi Level of Bi/InAs Interface

V.A. Golyashov[a], A.M. Shikin[b], I.I. Klimovskikh[b], Wu Shilong[c], A.Kimura[d], T.Okuda[c], O.E. Tereshchenko[a,d]

[a]*Institute of Semiconductor Physics Siberian Branch, Russian Academy of Sciences, pr.Akademika Lavrent'eva 13, Novosibirsk, 630090 Russian Federation*
[b]*Saint Petersburg State University, Saint Petersburg, 198504, Russian Federation*
[c]*Hiroshima Synchrotron Radiation Center, Hiroshima University, 2-313 Kagamiyama, Higashi-Hiroshima 739-0046, Japan*
[d]*Graduate School of Science, Hiroshima University, 1-3-1 Kagamiyama, Higashi-Hiroshima 739-8526, Japan*
[e]*Novosibirsk State University, ul.Pirogova2, Novosibirsk, 630090 Russian Federation*

Keywords: Bi, InAs, electronic structure, spin- and angle-resolved photoemission

In recent years a new field has emerged in condensed-matter physics based on the realization that the spin-orbit interaction can lead to spin-polarized electronic phases and on the prediction and observation of these phases at the interfaces. It is generally accepted that, Rashba spin-orbit coupling becomes larger in materials with heavier atoms due to the larger atomic spin-orbit coupling. The ultrathin film of group-V semimetal bismuth (Bi) is a promising candidate to investigate the graphene-like properties and surface Rashba effect, since the energy splitting of the bands is fairly large owing to the heavy atomic mass of the Bi atom. For the technological purposes InAs semiconductor is of special interest because it exhibits downward band bending leading to an accumulation of electrons at the surface, having characteristic of 2DEG. Such 2DEGs demonstrated many interesting and fundamental phenomena such as the integer and fractional Hall effect [1], 2D superconductivity [2] as well as technological importance in devices such as metal–oxide–semiconductor field-effect transistor (MOSFET) and high electron mobility transistor (HEMT). Another important and promising application is a spin-FET transistor based on InAs [3]. Such application is based on the Rashba effect in 2DEG that prescribes a lifting of the spin degeneracy in the presence of structural inversion asymmetry and strong spin-orbit coupling. In the spin- FET, spin modulation of the source-drain current relies crucially on controllability of the Rashba parameter. One of the possibility is to adjust Rashba parameter by forming interface between InAs and heavy atoms.

The aim of this work is to develop the methods of preparation (substrate surface preparation, evaporation rate, …) and to study the electronic structure of Bi/InAs(111) interfaces using state-of-the-art spin- and angular resolved photoemission spectroscopy (SR ARPES) with synchrotron radiation at BL-9B.

We have found that Bi deposition on InAs(111)A-(2x2) surface at room temperature (RT) led to the epitaxial growth with forming well-ordered (1x1) hexagonal Bi phase with the coverage above one monolayer. Figures 1(a) and (b) show the experimental band dispersion and its second derivative of bismuth monolayer on InAs(111)A surface. The dispersion measured by ARPES shows no gap at the surface, indicating surface metallization. The dispersion near the Fermi level (0-0.5 eV) is a typical for bismuth ultrathin film states characterized by Rashba-type [5]. To confirm that the observed Rashba like bands are spin polarized, we performed spin-resolved photoemission measurements at opposite wave vectors. Spin-resolved ARPES demonstrates the presence of spin-polarized states directly at the Fermi level [Fig. 1(c)]. Below the Fermi level these states crosses the gap of InAs forming linear dispersion with crossing point at 0.25 eV below the Fermi level. The presence of Bi-induced states in the gap of InAs with linear dispersion is similar to graphene with two important differences: states are spin-polarized and located at Γ point. It is found that the surface Fermi level position at InAs(111)A is unpinned and can be changed in controllable way by Bi adsorption- desorption process.
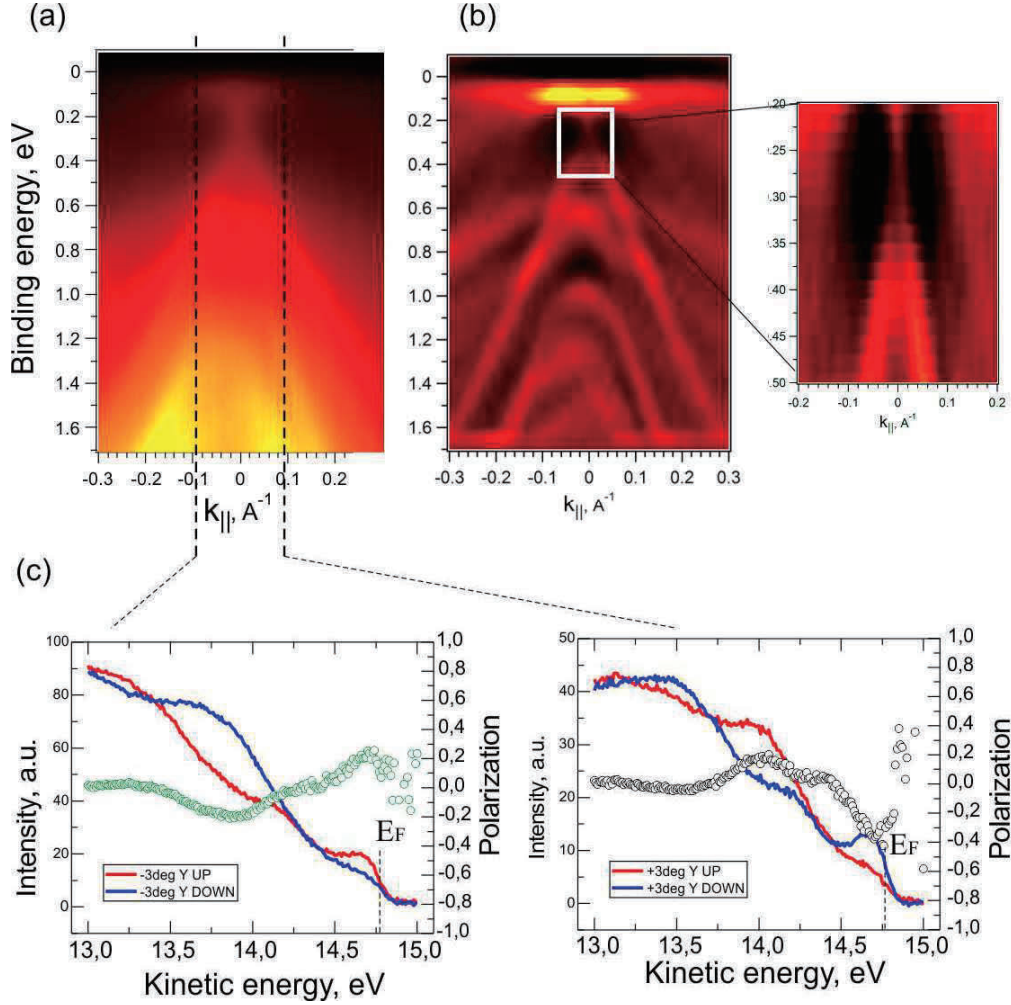
FIGURE 1. (a) Band structure of the bismuth monolayer on InAs(111)A surface along Γ-К. (b) Second derivative with respect to energy and zoom of Bi states in the energy gap of InAs. (c) Spin-resolved energy distribution curves measured at k=±0.1 A^{-1}.

Another behavior is observed when deposition takes place at elevated temperature. At 1 ML of Bi coverage the InAs(111)A-(2√3x3)Bi structure is formed which consist of three 60° oriented domains. The electronic structure of InAs(111)A-(2√3x3)Bi surface is significantly different from those observed on InAs(111)A-(1x1)Bi. First of all, the dispersion contains a small gap, which can be considered in the first approximation as a gap in the primarily Rashba states. The appearance of a gap is probably induced by the strong spin-orbit interaction in bismuth layer and reduced structural surface symmetry. In this case, the polarized states remain, and the presence of the gap may allow considering this system as a promising candidate for the spin-transistor system. The observed dispersion can also be interpreted as the graphene-like Dirac state with a gap. Moreover, 2D electron states in the quantized states at the InAs surface are hybridized with Bi states that should lead to increase of Rashba splitting in 2D states of InAs.

REFERENCES

1. K. von Klitzing, et al., Phys. Rev. Lett. 45, 494 (1980).
2. N. Reyren, et al., Science 317, 1196 (2007).
3. H. C. Koo, et al. Science, 325, 1515 (2009).
4. P. D. C. King, et al., Phys. Rev. Lett. 104, 256803 (2010).
5. T. Hirahara, J. of Electr. Spectr. and Rel. Phen. 201, 98 (2015).

Removal of phosphate by coal fly ash

Kyunghoi Kim[a], Kyeongmin Kim[a], Shinjiro Hayakawa[b]

[a]Department of Ocean Engineering, Pukyong National University, 45, Yongso-ro, Nam-Gu, Busan 48513, Republic of Korea
[b]Graduate School of Engineering, Hiroshima University, 4-1, Kagamiyama 1 chome, Higashi-Hiroshima 739-8527, Japan

Phosphate is essential for all living things. It also plays a vital role in agricultural and industrial development. However, substantial quantities of phosphate in water bodies owing to the discharge of wastewater (as low as 0.02 mg/L) can trigger eutrophication (Conley et al., 2009; Li et al., 2016). Therefore, treatment of wastewater is required to control the concentration of phosphate before its discharge. Fly ash is a byproduct of coal combustion in thermal electric power stations. Fly ash has recently attracted interest for wastewater treatment because of its physical and chemical properties, such as calcium oxide content. Furthermore, application of a byproduct in wastewater treatment is highly desirable in terms of economic advantages. In this study, removal mechanism of phosphate with coal fly ash was analyzed using X-ray absorption fine structure (XAFS) analysis.

XAFS analysis (beamline BL-11 of the Hiroshima Synchrotron Research Center, HiSOR) of the K-edge of calcium was performed for the precipitates with the components contained in the initial and reacted fly ash in phosphate solution. The standard spectra of calcium hydrogen phosphate, calcium oxide, and calcium hydroxide are shown in Figure 1, and curve fitting was carried out using analysis software.
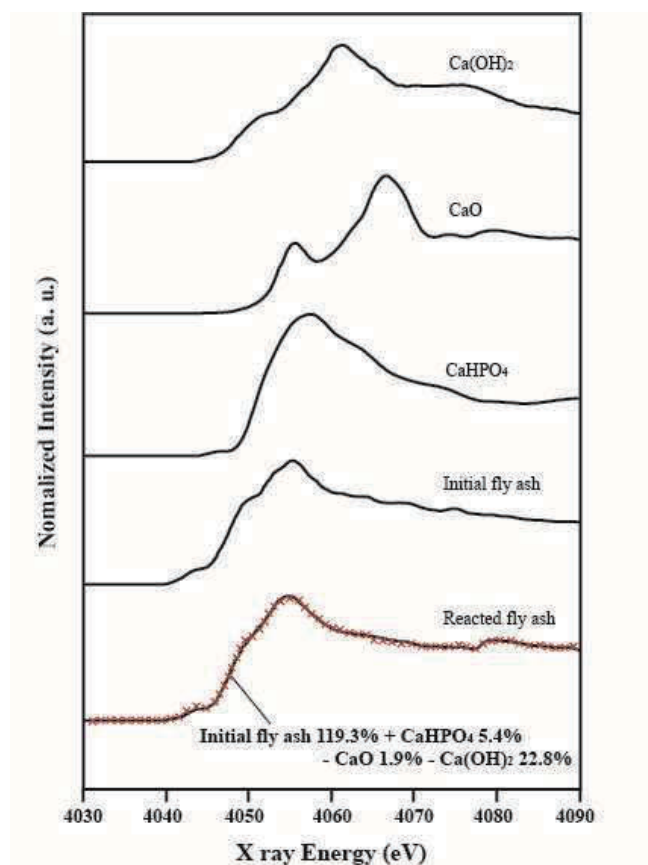

FIGURE 1. Calcium K-edge XANES spectra of the fly ash with several calcium standards.

The calcium K-edge curve of the initial fly ash has an inflection point at approximately 4050 eV, which corresponds to calcium hydroxide, which does not appear in the spectra of the reacted fly ash. This may imply that calcium hydroxide was decomposed in water to calcium ions. The curve fitting results clearly show that calcium hydrogen phosphate ($CaHPO_4$) formed on the surface of the reacted fly ash, whereas calcium oxide and hydroxide were hydrolyzed. The results of XAFS analysis proposed that calcium hydrogen phosphate is mainly formed as precipitates (Lu et al., 2009 and Xu et al., 2010).

$$Ca^{2+} + H^+ + PO_4^{3-} + 2H_2O \rightarrow CaHPO_4 \cdot 2H_2O \downarrow \tag{1}$$
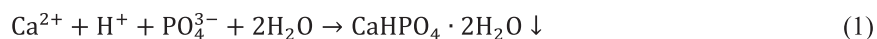
REFERENCES

1. Conley, D.J., Paerl, H.W., Howarth, R.W., Boesch, D.F., Seitzinger, S.P., Havens, K.E., Lancelot, C., Likens, G.E., 2009. Controlling eutrophication: nitrogen and phosphorus, Science 323, 1014–1015.
2. D. Xu et al., "Adsorption of Pb(II) from aqueous solution to MX-80 bentonite: effect of pH, ionic strength, foreign ions and temperature", *Appl. Clay Sci.* 2008, 41, 37–46.
3. Li, R., Wang, J.J., Zhou, B., Awasthi, M.K., Ali, A., Zhang, Z., Lahori, A.H., Mahar, A., 2016. Recovery of phosphate from aqueous solution by magnesium oxide decorated magnetic biochar and its potential as phosphate-based fertilizer substitute, Bioresour. Technol. 215, 209–214.
4. S.G. Lu et al., "Removal mechanism of phosphate from aqueous solution by fly ash", *J. Hazard. Mater.* 2009, 161, 95–101.

Identifying sulfur species in particulate matter derived from various ships using XAFS analyses

Satoshi ASAOKA[a], Waqar Azeem JADOON[a], Tomoshisa DAN[b],
Hideo OKAMURA[a], Kadumitsu NAKAGUCHI[c], Mitsuru KUBOTA[c]
Ayaka TAMURA[d] and Shinjiro HAYAKAWA[d]

[a] *Research Center for Inland Seas, Kobe Univ. (5-1-1 Fukaeminami Higashinada Kobe 658-0022 Japan)*
[b] *Graduate School of Maritime Sciences, Kobe Univ. (5-1-1 Fukaeminami Higashinada Kobe 658-0022 Japan)*
[c] *TOYOSHIO MARU, School of Applied Biological Sciences, Hiroshima Univ. (7-4 Takaramachi, Kure 737-0029 Japan)*
[d] *Graduate School of Engineering, Hiroshima Univ. (1-4-1 Kagamiyama, Higashi-Hiroshima 739-8527 Japan)*

Keywords: Acid rain, Diesel engine, Exhaust gas, Fuels, Soot

Introduction

Particle matters (PM) from ships affect the ocean environment on various scales. Additionally, PM and sulfur can also have indirect effects on climate through changes in global radiative forcing [1]. The estimated annual PM emission from ships is 0.9 to 1.7 million tons [2]. It is assumed that combustion of ship fuel emits sulfur as SO_x (SO_2 and SO_3) with other exhaust gases. The SO_x is partially adsorbed as sulfate onto PM through hydration processes due to decrease in the temperature of the exhaust gas. Given that the emission of PM and sulfur is well related to ship fuels, the International Maritime Organization (IMO) in 2015 regulated the sulfur contents in ships fuel less than 3.5% and 0.1% for general and designated sea areas, respectively. In 2020, the regulation will further be strengthened and reduce sulfur content in ship fuel to 0.5% for general sea areas.

Although, sulfur adsorbed on PM in exhaust gases from fuels is considered to be sulfate [2]. However, chemical species of sulfur adsorbed on PM in exhaust gases are not well known. The purpose of this study is to identify sulfur species adsorbed on PM in exhaust gases using XAFS.

Materials and Methods

PM samples were collected from a container carrier 'EMERALD 1'(Aoki Marine Co., Ltd.), a tugboat 'KASUGA-MARU II' (MARUEI Co., Ltd.), a research and training electric propulsion vessel 'TOYOSHIO-MARU' (Hiroshima University) and a training vessel 'HIROSHIMA-MARU' (National Institute of Technology, Hiroshima College) (**Table 1**). PM in the engine exhaust gas from 'EMERALD I' was collected on a glass fiber filter (GFF; PG-60; Advantec) by letting 10 L of the exhaust gas pass through GFF into a filter manifold chamber using an air pump. The mass of PM collected on GFF was calculated by weight difference before and after introducing the exhaust gas. In other ships soot samples were scraped from their funnels.

Table 1 Vessels used in this study to collect PM samples

Vessel name	Vessel Type	Tonnage (T)	Rated output (kW)	Fuels
EMERALD I	Container carrier	5215 (DWT)	1470 x 2	A-type heavy oil
KASUGA-Maru II	Tagboat	19 (GT)	810	A-type heavy oil
TOYOSHIO-Maru	Research and Training	400 (GT)	441 x 3	A-type heavy oil
HIROSHIMA-Maru	Training	769 (GT)	956	Light oil

XAFS analyses of the PM samples were conducted using the BL11 of Hiroshima Synchrotron Research Center. The synchrotron radiation from a bending magnet was monochromatized with a Si (111) double-crystal monochromator. The sample chamber was filled with He gas. The XAFS spectra were measured in two different modes simultaneously, i.e. the x-ray fluorescence yield using XR-100FAST SDD (Amptek) and the conversion electron yield. The incident X-rays energy was calibrated with CEY mode obtained S K-edge XAFS spectrum of $CuSO_4 \cdot 5H_2O$ and the main peak corresponding to the sulfate was set at 2481.6 eV. Each sample was mounted on a double-stick tape (NW-K15; Nichiban) placed in the central hole (15 mm in diameter) of a copper plate. The angle between the incident x-rays and the sample surface was 20 degree. The X-ray fluorescence was

detected from the direction normal to the incident beam in the plane of electron orbit of the storage ring. The X-ray window of the detector (C1 model) utilizes silicon nitride (Si_3N_4) with an aluminum coating to extend the low energy response down to carbon. The total sulfur content in PM was also measured by ICP-AES after wet digestion.

Results and Discussion

The sulfur species in soot mainly identified as sulfate, alkyl sulfonate and C-S bond derived from heavy oil (**Fig. 1**). Total sulfur content in soot from HIROSHIMA-MARU was significantly low compared to other ships, and the alkyl sulfonate and C-S bond were not identified. This could be due to the use of light oil in the HIROSHIMA-MARU and sulfur content in the light oil is much lower (0.0006%) than A-type heavy oil (0.79-0.85%). The electric propulsion vessel 'TOYOSHIO-MARU was second lowest in terms of sulfur content in soot even though the vessel was operated by A-type heavy oil. This ship is using heavy oil for electricity generation to run the engine. The low sulfur content could be resulted its low emissions from generator compared with ship engine. The composition of sulfur species did not significantly change under the 44% and 64% load of generator operation condition.

PM concentration in exhaust gas from EMERALD I and sulfur concentration in the PM are shown in **Fig. 2**. The engine in EMERALD I was operated at 85% and 50% load that represented full and half navigation, respectively. The PM concentration in exhaust gas at half navigation reduced to 21% compared with full navigation. However, the sulfate and alkyl sulfonate contained PM did not decrease significantly. Therefore, this PM decrease was considered mainly due to decrease in carbon and SOF fraction.
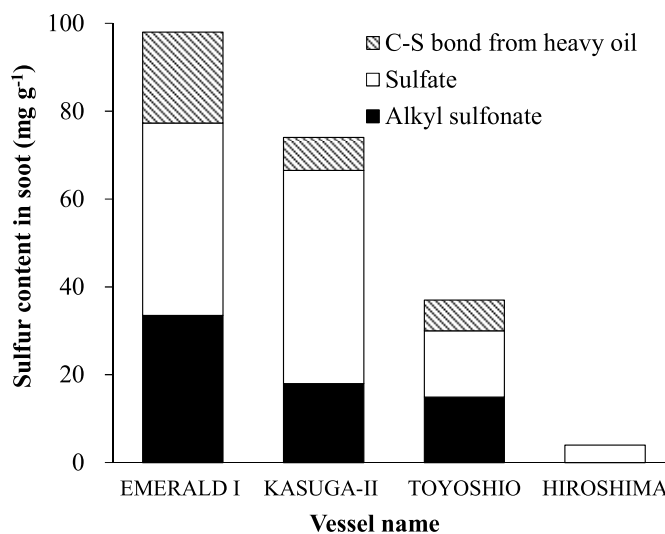

Fig. 1 Sulfur species content in soot collected from various vessels.
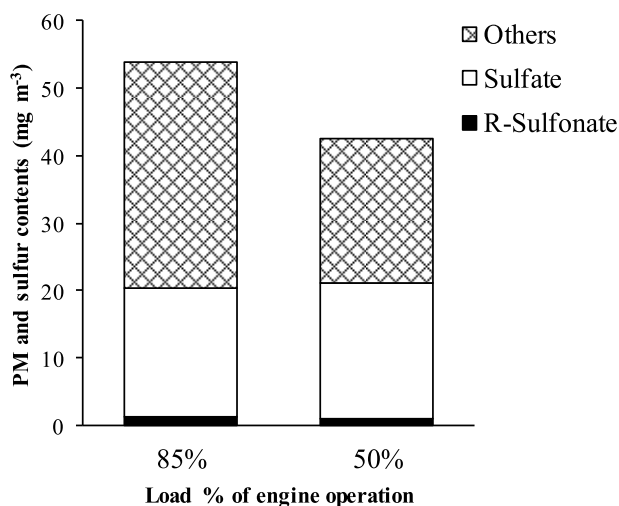
Fig. 2 PM Concentration in exhaust gas and sulfur species content in PM from EMERADL I

Acknowledgement

References

1. C. Kevin, J. C. James, K. Prasad, F. Paul and N. P. Spyros, *Nature*, **400**, 743-746, (1999).
2. J. Moldanová E. Fridell O. Popovicheva, B. Demirdjian, V. Tishkova, A. Faccinetto and C. Focsa, *Atmosph. Environ.* **43**, 2632-2641 (2009).

Speciation of sulfur in long transport materials from China

Shoji Imai[a], Yuhei Yamamoto[a], Takashi Yamamoto[a]

[a]*Graduate School of Technology, Industrial and Social Science, Tokushima University, Tokushima 770-8506, Japan*

Keywords: insoluble sulfur, long transport of atmospheric pollutant, speciation.

Aerosol particles as atmospheric pollutants transported from the east part of Asian continent including China have been paid attention in terms of transboundary environmental problem. Sulfur is one of the major pollutants in aerosol particles [1]. Coal burning is a major anthropogenic sulfur origin at the east part of Asian continent. Large fraction of atmospheric sulfur is contained in aqueous phase through rain and wash out due to solubility. Therefore, many studies reported soluble sulfur in atmospheric deposition, but there are few studies on insoluble sulfur species [2]. Although insoluble fraction also contains anthropogenic sulfur, origin and fate of insoluble sulfur in aerosol particles are still unclear. It is expected that there are differences on the chemical state of sulfur from anthropogenic and natural sources [3]. In this study, we investigated oxidation number of sulfur in aerosol particles using sulfur K-edge XAFS at HiSOR BL-11 in order to discuss the origin and fate of insoluble sulfur.

Aerosol particles were collected from snow and rime samples at remote mountain areas in Japan, where contribution from domestic urban area was neglect. In winter season, contribution of atmospheric pollutants transported from the east part of Asian continent becomes larger because of the monsoon of the eastern Asian area. Snow and rime samples were collected using specific samplers to prevent contamination. Collected snow and rime samples were filtered by a 0.45 μm membrane after melting. Aerosol particles on the membrane filters were employed for XAFS experiment. XAFS spectrum of aerosol particles was measured by fluorescence mode using a silicon drift detector. The observed X-ray absorbance data were analyzed using IFFEFIT [4].

Figure 1 showed sulfur K-edge XANES spectra of aerosol particles and coal ash as a reference material. Broken lines denoted the peak top energy positions of cystine (-2) and Na_2SO_4 (+6) as reference materials. For rime samples (Fig. 1 a~d), the peak top energy positions of the two peaks were consistent with those of cystine and Na_2SO_4, suggesting that sulfur in rime was mixture of -2 and +6 species. For snow samples (Fig. 1 e~g), the spectra showed two peaks as well as rime samples. The spectra of coal ash was remarkably resemble with those of rime and snow samples. There is a possibility that origin of sulfur species in rime and snow samples was coal burning at the east part of Asian continent.
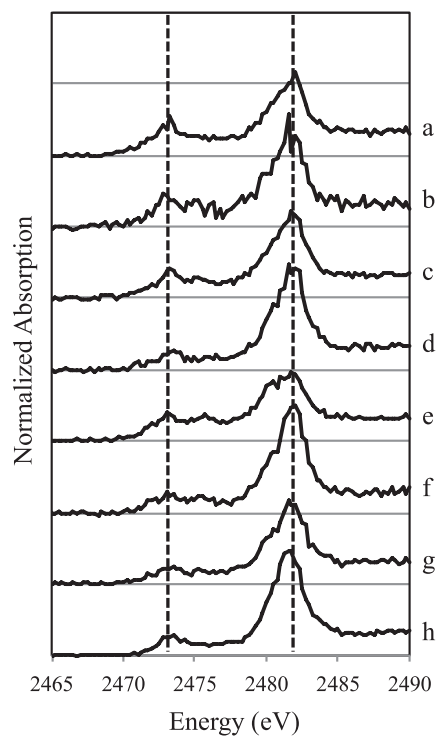
FIGURE 1. Sulfur K-edge XANES spectra of aerosol particles in rime and snow. a) rime at Mt. Kajigamori, Kouchi Pref. 2014, Jan. 5; b) rime at Mt.Kajigamori, 2014, Feb. 16; c) rime at Mt. Kajigamori, 2014, Feb. 21; d) hard rime at Mt. Kajigamori, 2013, Dec. 28; e) snow at Kajigamori, 2016, Jan. 25; f) snow at Mt. Hiruzen, Okayama Pref. 2014, Jan. 29; g) snow at Mt. Iwate, Iwate Pref. 2014, Jan. 31; h) coal ash. Left hand broken lines was the peak top energy position of cystine, whereas right hand one was Na_2SO_4.

REFERENCES

1. S. Ishibashi and H. Hayami, *J. Japan Soc. Atmosph. Environ.*, 2015, **50**, 138.
2. T. Tanabe et al., *Bunseki Kagaku*, 2004, **53**, 1411.
3. Y. Ban et al., *J. Japan Soc. Air Pollut.*, 1985, **20**, 470.
4. B. Ravel and M. Newville., *J. Sync. Rad.*, 2005, **12**, 537.

Simultaneous detection of X-ray fluorescence and conversion electrons
– extension to X-ray fluorescence of carbon and oxygen –

Yuta Hamashima[a], Alvaro Munoz Noval[a], Ayaka Tamura[a],
and Shinjiro Hayakawa[a]

a Department of Applied Chemistry, Graduate School of Engineering, Hiroshima University, Hiroshima, Japan

Keywords : XFY, CEY, SDD with Si_3N_4 thin film window, light elements

Introduction

X-ray fluorescence yield (XFY) and conversion electron yield (CEY) can be measured simultaneously from a sample in a He filled chamber at BL11. To collect CEY in the He environment, an electrode that is transparent to X-ray fluorescence above 1 keV was placed 8 mm from the sample surface, and XFY was collected through the electrode. The electrode was made of 6 μm thick polypropylene (PP), and the 10 nm of copper was deposited onto the surface of PP. We have introduced a new silicon drift detector (SDD) with a 90 nm thick Si_3N_4 window to expand the applicable elemental range down to C and N. However, the transmittance of the thin film electrode was insufficient (0.4 %) for O Ka. In this work, we report on the revised detection system for the simultaneous recording of conversion electrons and X-ray fluorescence of light elements by introducing a new electrode. The combination of both techniques seems a very attractive method for the study of light elements in samples.

Experimental

Experiments were performed on the BL-11. The beamline is equipped with a Si(111) double crystal monochromator, and monochromatized X-rays from 2.1 to 5.9 keV are available. X-ray fluorescence from the sample is monitored with a SDD. The new SDD (FAST SDD, Amptek) is equipped with a 90 nm thick Si_3N_4 (C1) window. The technical specifications from the manufacturer set a transmittance of 29.4% for O Ka (0.525 keV).

As the new electrode, we adopted a home-made copper electrode of 0.7 mm in thickness with a 5 mm×15 mm hole. This hole has the sufficient size for detecting X-ray fluorescence from the sample while maintain the electric field on the sample to prevent created ion-electron paris from recombination.

A disk of quartz (SiO_2) was utilized as a reference material of infinite thickness for qualitative analysis of O. A 150 nm film of silver deposited on Si wafer was employed for evaluation of electrode. The CEY was measured as the current flowing from the sample to the earth during X-ray irradiation, and the bias dependency of the current from 0 to 100 V.

Ag L_3-edge XAFS spectra was measured to confirm whether edge jump can be observed in CEY mode using the new electrode.

Results and Discussion

Figure 1 shows the comparison of XRF spectra of a disk of quartz (SiO_2) using both the thin film electrode (Previous electrode) and the electrode with a hole (New electrode). It was clear that the attenuation of X-ray fluorescence through the previous electrode was completely removed, and the detection of O Ka was realized. Cu Lα (0.930keV) peak in the spectrum might be attributed to the copper plate to fix the sample.

In Figure 2, the bias dependency of the new electrode and the previous electrode is depicted. CEY current detected by the new electrode was less than that of the previous electrode. However, it was confirmed that the detected CEY reached a constant value beyond 40 V with both electrodes. In this plateau (Ion chamber region), conversion electrons are collected without the recombination.

Figure 3 presents the Ag L_3-edge XAFS spectra from Ag (150nm)/Si, Both XFY and CEY were detected simultaneously by using the new electrode, and the qualities of the spectra were sufficient.
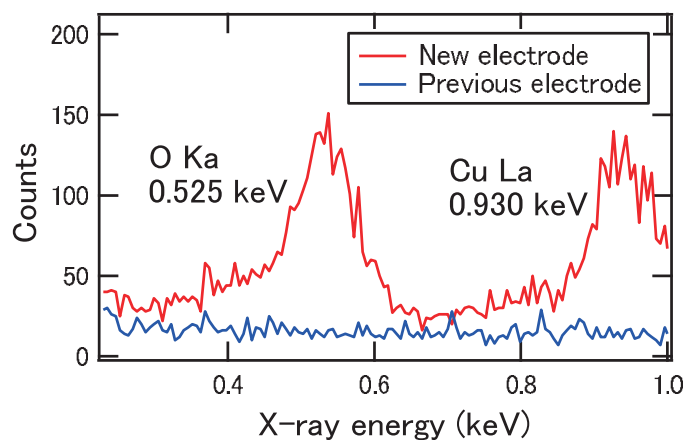
FIGURE 1. XRF spectra of a disk of quartz (SiO_2) obtained by the SDD with the 90 nm Si_3N_4 window using the old electrode and the new electrode presented in this work. The incident X-ray energy was 2.9 keV, and the data acquisition time was 1000 s.
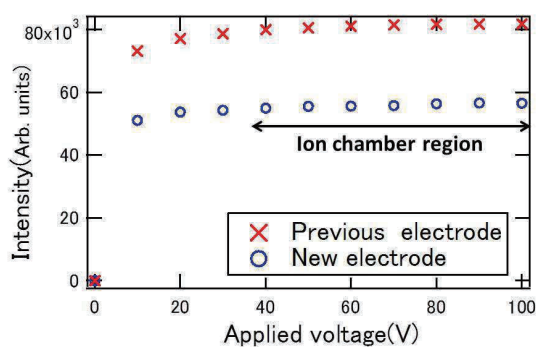
FIGURE 2. Bias dependency of the previous and new electrode. Sample was Ag(150nm)/Si. The incident X-ray energy was 2.9 keV, and each plot acquisition time was 10 s.
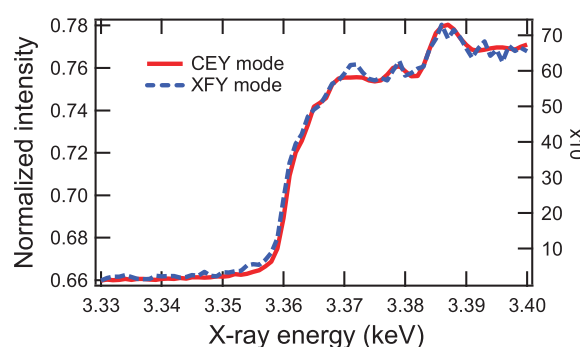
FIGURE 3. Ag L_3-edge XAFS Ag(150nm)/Si. XFY was monitored with the SDD. CEY was detected by the new electrode.

Oxidation mechanism of hydrogen sulfide on the surface of mixture of granulated coal ash and metal oxides

Waqar Azeem JADOON[a], Satoshi ASAOKA[a], Kenji NAKAMOTO[b],
Kazutoshi HINO[b], Ayaka TAMURA[c] and Shinjiro HAYAKAWA[c]

[a] Research Center for Inland Seas, Kobe University (5-1-1 Fukaeminami Higashinada Kobe 658-0022 Japan)
[b] The Chugoku Electric Power Co. Inc. (4-33 Komachi, Naka-ku, Hiroshima-shi, Hiroshima 730-8701 Japan)
[c] Graduate School of Engineering, Hiroshima University (1-4-1 Kagamiyama, Higashi-Hiroshima 739-8527 Japan)

1. Introduction

High concentration of toxic hydrogen sulfide was detected in eutrophic enclosed water bodies. Therefore, hydrogen sulfide removal from eutrophic marine sediments is imperative to maintain healthy ecosystems and support aquaculture activities. We developed granulated coal ash (GCA) by mixing fly ash (from a coal electric power plant) and blast furnace cement for the remediation of eutrophic marine sediments. The GCA removed hydrogen sulfide effectively from marine sediments [1,2]. However, the achieved hydrogen sulfide removal rate is insufficient to be replicated in industries such as wastewater treatment plants, geothermal power plants and oil refineries to remove hydrogen sulfide at faster rates. The improved hydrogen sulfide removal rate was obtained by the addition of metal oxides to the original GCA. This study aims to identify sulfur species in metal oxide added GCA prototypes to understand the hydrogen sulfide removal mechanisms.

2. Materials and Methods

The GCA prototypes were prepared by adding coal fly ash (87wt%) to blast furnace cement (13wt%); and coal fly ash and blast furnace cement to CuO or NiO or Riboflavin amounting 0.1, 1 and 10wt%, respectively of the coal fly ash and blast furnace cement mixture. The batch experiments were carried out to obtain the removal rates of hydrogen sulfide by GCA prototypes. Hydrogen sulfide solutions (10 and 100 mg-S L^{-1}) were prepared in 30 mmol L^{-1} Tris–HCl buffer (Kanto Kagaku), each of pH 8.2. The buffer solution was purged with N_2 gas prior to the addition of $Na_2S \cdot 9H_2O$ (Wako Pure Chemical Industries) to remove the dissolved oxygen. 0.2 g GCA prototypes were briefly added to 100 mL sealable glass vials that were afterward gently dispensed with 50 mL of hydrogen sulfide solution. Subsequently, the headspaces of these vials were replaced with N_2 gas and the vials were sealed with rubber corks. Thereafter, vials were agitated moderately (100 rpm) at 25 ºC in an oven under anoxic conditions. The changes of hydrogen sulfide concentrations with respect to time were measured using a detection tube (200SB: Komyo Rikagaku Kougyo). These batch experiments were conducted in triplicate. The wet electrodes were used to measure the pH and Eh of the solutions before and after hydrogen sulfide removal.

Sulfur K edge XAFS spectra (ranges 2460–2490 eV) were measured using the BL11 in the Hiroshima Synchrotron Research Center (HiSOR). The synchrotron radiation from a bending magnet was monochromatized with a Si (111) double-crystal monochromator. The sample chamber was filled with He gas. The XAFS spectra were measured by the X-ray fluorescence yield (XFY) mode using a SDD detector (XR-100FAST; AMPTEK). The X-ray window of the detector (C1 model) utilizes silicon nitride (Si_3N_4) with an aluminum coating to extend the low energy response down to carbon. The CEY mode obtained spectra of $CuSO_4 \cdot 5H_2O$ were used to calibrate the incident X-ray energy around K edges of sulfur. The K edge main peak of sulfate was set to 2481.6 eV. Relatively flat GCA prototype samples prepared in hydrogen sulfide solution of 100 mg-S L^{-1} concentration were mounted on a double stick tape (NW-K15; Nichiban) placed in the central hole (15 mm in diameter) of a copper plate. Incident X-ray angle to the sample surface was adjusted to 20 degrees and the X-ray fluorescence was detected from the direction normal to the incident beam in the plane of electron orbit of the storage ring.

3. Results and Discussion

In the case of 10 mg-S L^{-1} as the initial concentration of hydrogen sulfide, the first order rate constants for hydrogen sulfide (h^{-1}) reached almost maximum when 0.1wt% of NiO, 1wt% of Riboflavin and 10wt% of CuO were added to the coal fly ash and the cement mixture, respectively (**Fig. 1**). The removal rate of hydrogen sulfide did not increase significantly, despite the dosage increasing from 0.1wt% to 1wt% for NiO and Riboflavin, respectively. The removal rate obtained by the CuO added prototype only improved at its 10 wt% addition to the ash and cement mixture.

The Sulfur K edge spectra of several sulfur standards and the GCA prototype with NiO (1wt%) before and after removal of hydrogen sulfide are shown in **Fig. 2**. The peak around 2482eV represents sulfur derived from coal. The new peak around 2472 eV was observed after the removal of hydrogen sulfide. The peak at 2472 eV was identified as sulfur. The NiS was not identified because the Eh of hydrogen sulfide solution ranged from -178 to -188 mV, which is higher than the required Eh value to form NiS. Absence of NiS in the NiO and Riboflavin added GCA implies that NiO did not directly remove hydrogen sulfide. The Sulfur K edge spectra of the GCA prototype with Riboflavin (1wt%) before and after removal of hydrogen sulfide are shown in **Fig. 3**. The new peak around 2472 eV, which represents sulfur, was also observed after the removal of hydrogen sulfide. We already reported that the hydrogen sulfide was removed through the oxidation to sulfur by the manganese oxide contained in the GCA [1,2]. It is possible that the addition of NiO and Riboflavin might work as an electron mediator to the oxidation of hydrogen sulfide by the manganese oxide in the GCA prototype.
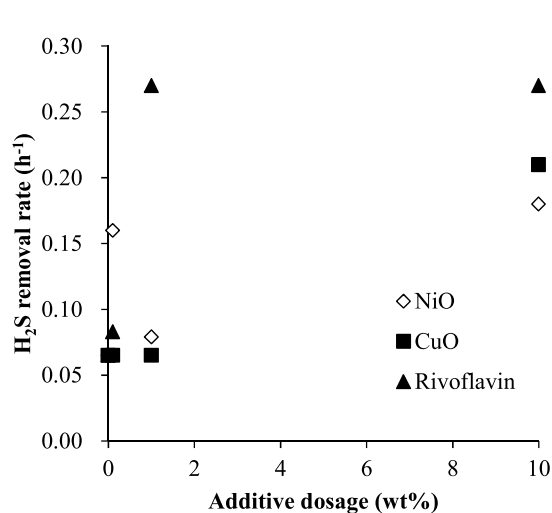

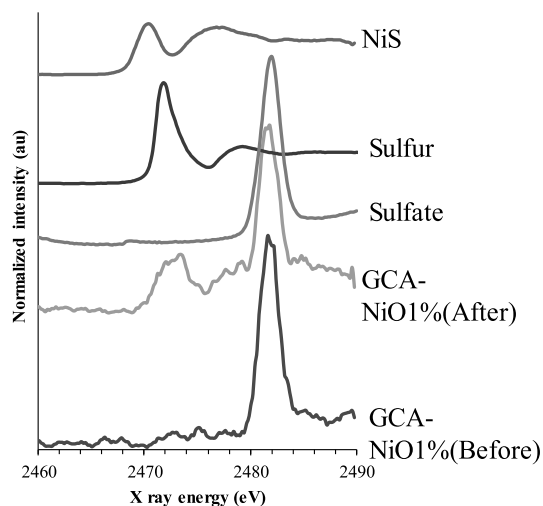Fig.1 Removal rate of hydrogen sulfide obtained by the GCA prototypes .

Fig. 2 Sulfur K edge XANES spectra of the GCA prototypes with NiO(1wt%) before and after hydrogen sulfide removal

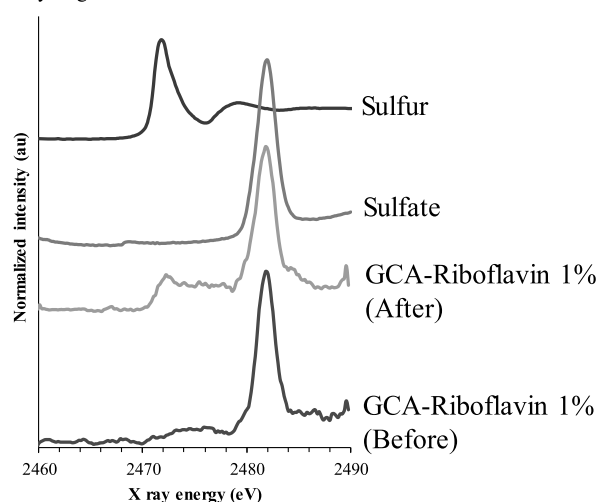Fig. 3 Sulfur K edge XANES spectra of the GCA prototypes with Riboflavin(1wt%) before and after hydrogen sulfide removal

REFERENCES

1. Asaoka S., et al., *Chem. Eng. J.*, 254, 531-537(2014)
2. Asaoka S., et al., *J. Colloid Interf. Sci.*, 377, 284-290(2012).

Conformation of Membrane-Bound Myelin Basic Protein Characterized by Vacuum-Ultraviolet Circular-Dichroism Spectroscopy

Munehiro Kumashiro, Koichi Matsuo, Yudai Izumi, Hirofumi Namatame, Masaki Taniguchi

Hiroshima Synchrotron Radiation Center, Hiroshima University, Japan

Keywords: liposome; myelin basic protein; protein–membrane interaction; secondary structures; synchrotron-radiation circular dichroism

Myelin basic protein (MBP) is a membrane-bound protein which contributes to myelination of the membrane surrounding the axon of neuron cell [1]. Since MBP in the myelin membrane enhances the signal transduction in the cell, the isolation of MBP from the membrane causes various severe diseases related to the demyelination. Hence elucidating the interaction mechanism between MBP and membrane would be useful for understanding myelination and demyelination phenomena. It is known that MBP is intrinsically disordered protein in aqueous solution (or native state) and increases the helical contents when interacting with membrane. However MBP conformation in the membrane and the interaction mechanism between MBP and membrane remain unclear. A vacuum-ultraviolet circular dichroism (VUVCD) spectroscopy has a great advantage in analyzing the protein secondary structures because this spectroscopy can extend the protein CD spectra down to 160 nm by using a synchrotron radiation [2,3]. Further this technique is applicable to the experiments in various solvent conditions such as membrane solution. In this study, to characterize the conformation of membrane-bound MBP, we measured the VUVCD spectra of MBP interacted with various lipid liposomes related to myelin membrane and discussed the mechanism of MBP-membrane interactions.

Myelin membrane is composed of various lipid molecules such as phosphatidylcholine (PC), phosphatidylethanolamine (PE), phosphatidylserine (PS), phosphatidylinositol (PI), and sphingomyelin (SM). Each lipid liposome was prepared by an extrusion technique and mixed with MBP solution. The VUVCD spectrum of MBP without liposome vesicle (native state) exhibited a large negative peak around 190 nm. This spectrum did not change when adding the PC, PE, and SM liposome vesicles, meaning that MBP had no structural change in these three liposomes. On the other hand, the spectra of MBP in the PS and PI liposome vesicles showed two negative peaks around 208 and 222 nm, and a positive peak around 190 nm, suggesting that the helical structure of MBP increased in the both liposomes. The VUVCD analysis coupled with a neural-network method revealed that MBP in the PS and PI liposome vesicles formed six helical regions on the amino-acid sequence, and five in six regions were negatively charged helices. Liposome surfaces of PC, PE, and SM are uncharged while those of PS and PI are positively charged. These results suggest that the MBP-membrane interaction is mainly caused by the electrostatic interaction and the interaction induces the formation of helical structures in MBP.

Reference
1. J. M. Boggs, *Cell. Mol. Life Sci.* **2006**, 63, 1945.
2. K. Matsuo, H. Watanabe, K. Gekko, *Proteins* **2008**, 73, 104.
3. K. Matsuo, Y. Maki, H. Namatame, M. Taniguchi, K. Gekko, *Proteins* **2016**, 84, 349.

Circular Dichroism of Bio-organic Materials Irradiated by Vacuum-Ultraviolet Circularly-Polarized Undulator Light

Jun-ichi Takahashi[a], Natsumi Suzuki[a], Yoko Kebukawa[a], Kensei Kobayashi[a], Masaki Fujimoto[b], Masahoro Katoh[b], Yudai Izumi[c], Koichi Matsuo[c]

[a]Fucalty of Engineering, Yokohama National University, Yokohama 250-8501, Japan
[b]UVSOR Facility, Institute for Molecular Science, Okazaki 444-8585, Japan
[c]Hiroshima Synchrotron Radiation Center, Higashi-Hiroshima 739-0046, Japan

Keywords: Circular Dichroism, Homochirality, Amino Acids.

The origin of terrestrial bio-organic homochirality (L-amino acid and D-sugar dominant) is one of the most mysterious issues that remain unresolved in the study of the origin of life. Because bio-organic compounds synthesized in abiotic circumstances are intrinsically racemic mixtures of equal amounts of L- and D-bodies, it is hypothesized that chiral products originated from asymmetric chemical reactions induced by a "chiral impulse". These types of asymmetric reactions could have possibly been derived from physically asymmetric excitation sources in space and the chiral products would have been transported to primitive Earth resulting in terrestrial homochirality (Cosmic Scenario) [1]. In space, asymmetric excitation would be mainly effectuated by polarized photons of synchrotron radiation (SR) from kinetic electrons captured by strong magnetic field around neutron stars or white dwarfs in supernova explosion area, or by polarized photons scattered by interstellar dust clouds in star formation areas (Fig.1). Eventually, several terrestrial observations of polarized photon radiation from space due to scattering by interstellar dust clouds in star formation regions have been reported [2].

Several experiments have already examined asymmetric photochemical reactions in simple biochemical molecules by using circularly polarized light (CPL). We have already reported optical activity emergence in solid-phase films of racemic mixtures of amino acids by using CPL from UVSOR-II free electron laser (FEL) [3].

In this report, optical activity emergence into the achiral (optically inactive) amino acid film by using CPL from undulator beam line is demonstrated. We formed thin solid films of racemic mixture of alanine on fused quartz substrates from crystal powders of DL-alanine using a thermal-crucible vacuum evaporator. Sublimation temperature was 150~200°C and pressure of the vacuum chamber was approximately 10^{-2} Pa throughout the evaporation process. To introduce optical asymmetry into the racemic film, we irradiate them with CPL introduced from undulator beam line BL1U of UVSOR-III (Fig.2). The irradiated CPL wavelength was 215nm and total irradiation energies were 12 and 20 milliwatt-hour.

In order to clarify the optical activity of the films induced by CPL irradiation, we measured circular dichroism (CD) spectra using a commercial CD spectrometer (JASCO J-720WI). The dependence of the spectra on sample rotation angle of 0 and 90 degree-rotations was measured. If linear dichroism (LD) and/or linear birefringence (LB) components are dominantly effective, the signs of appearance CD peaks should be inverted. We ensured that rough spectrum profile and at least signs of two CD peaks were not changed. Therefore, observed appearance CD should be derived dominantly from chiral CD component. As a

result, almost completely symmetric spectra were observed with left- and right-handed CPL irradiation from undulator. These results are consistent with the results of CPL irradiation from FEL [3].

We are presently planning measurements of the dependence of CD spectra on irradiated CPL wavelength using SR-CD beamline (BL-12) of Hiroshima Synchrotron Radiation Center (HiSOR) over the shorter wavelength region than those with commercial CD spectrometer.
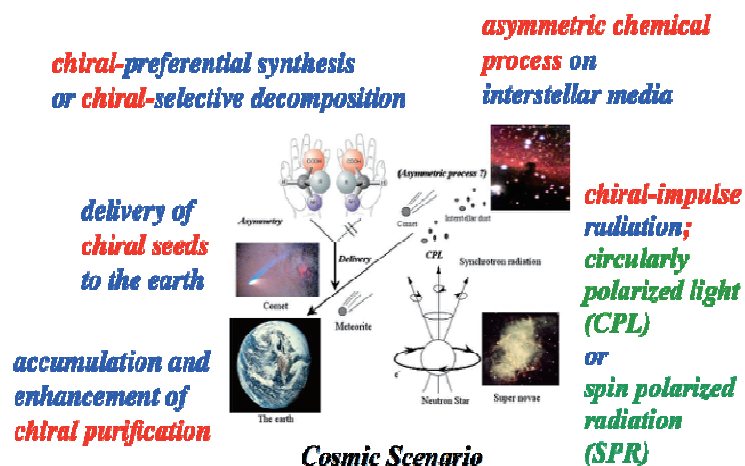

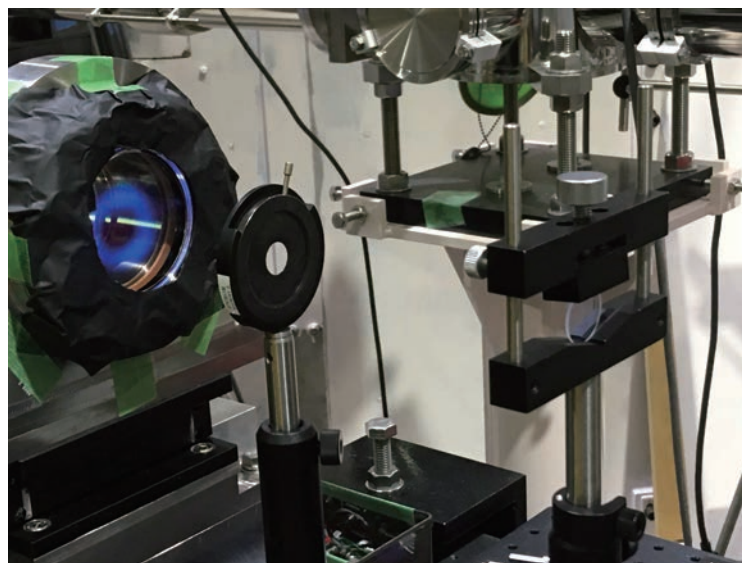**FIGURE 1.** Cosmic scenario for the origin of terrestrial bio-organic homochirality.

FIGURE 2. Photo of the irradiation experiment of circularly polarized light on BL1U of UVSOR-III.

REFERENCES

1. W. A. Bonner, *Origins Life Evol. Biosphere* **21**, 407-420 (1991).
2. T. Fukue, M. Tamura, R. Kandori, N. Kusakabe, J. H. Hough, J. Bailey, D. C. B. Whittet, P.W.Lucus, Y. Nakajima, J. Hashimoto, *Origins Life Evol. Biosphere* **40**, 335-346 (2010).
3. J. Takahashi, H. Shinojima, M. Seyama, Y. Ueno, T. Kaneko, K. Kobayashi, H. Mita, M. Adachi, M. Hosaka, M. Katoh, *Int. J. Mol. Sci.* **10**, 3044- (2009)

Conformations of α₁-acid glycoprotein fragments in membrane-bound state revealed by vacuum-ultraviolet circular-dichroism spectroscopy

Koichi Matsuo

Hiroshima Synchrotron Radiation Center, Hiroshima University, Japan

α₁-Acid glycoprotein (AGP) interacts with bio-membrane to change the conformation (β→α transition) and decrease the drug (hormone)-binding capacity. Hence, this conformational change of AGP coupled with the release of drugs into the membrane or cell is considered as a protein-mediated uptake mechanism of drugs (1). Previous our paper suggested that two peptide regions on the amino-acid sequence of AGP should strongly interact with liposome membrane, forming α-helical structures (1). Hence, the membrane-bound conformations of the two peptide fragments would provide any crucial hint on the membrane-binding mechanism of full-length AGP, which remains unclear. In this study, we measured the vacuum-ultraviolet circular-dichroism (VUVCD) spectra of two peptide fragments of AGP in the presence of the dimyristoyl phosphatidylglycerol (DMPG) liposomes at pH 4.5 to characterize these peptide conformations.

The amino-acid sequences of two peptide fragments (A- and G- peptides) were described in Figure 1. Figure 2 shows VUVCD spectra of A- and G-peptides at pH 4.5 and in the presence of DMPG liposomes. A-peptide at pH 4.5 with and without liposome showed small positive CD peak around 230 nm, which would be ascribed to the perturbation of aromatic side chain of tryptophane residue. Evidently, by adding the liposome, A-peptide had a large spectral change while G-peptide kept its spectra or conformations (unordered structure). Although A-peptide in the membrane-bound state exhibited a CD spectrum similar to β-rich protein, these results imply that the affinity of A-peptide to liposome is stronger than G-peptide, and that the liposome might bind to the A-peptide region of AGP before the G-peptide one.

A-peptide   G-peptide
NATLDQITGKWFY   WKKDKCEPLEKQHEKE

Figure 1. Amino-acid sequences of two peptide fragments.
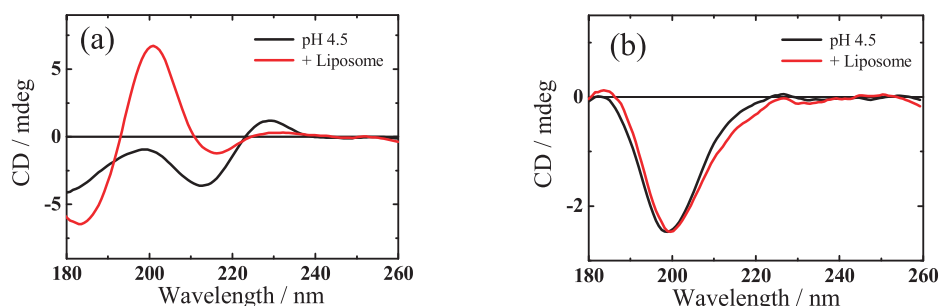
Figure 2. VUVCD spectra of A-peptide (a) and G-peptide (b) at pH 4.5 and in the presence of DMPG liposome.

References

1.   K. Nishi, T. Maruyama, H. B. Halsall, T. Handa, M. Otagiri, *Biochemistry* **2004**, 43, 10513.
2.   K. Matsuo, H. Namatame, M. Taniguchi, K. Gekko, *Biochemistry*, **2009**, 48, 9103.

Vacuum-Ultraviolet Circular Dichroism of Locust Bean Gum

Yasuyuki Maki[a], Ryo Takeda[a] and Koichi Matsuo[b]

[a]*Division of Molecular Science, Graduate School of Science and Technology, Gunma University, Kiryu 376-8515*
[b]*Hiroshima Synchrotron Radiation Center, Hiroshima University, Higashi-Hiroshia 739-8526*

**Keywords:** polysaccharides, vacuum ultraviolet circular dichroism, synergistic effect

Gels used in foodstuffs are usually multi-component systems such as mixtures of proteins and polysaccharides. In some cases, gels of these mixtures show a synergistic effect, that is, enhanced mechanical properties at a certain mixing ratio or gelation at concentrations below the gelation concentration of pure components. The synergistic effect has been applied to gelling agents used in food industries.

For example, mixtures of xanthan gum (XG) and locust bean gum (LBG), polysaccharides secreted from the bacterium *Xanthomonas campestris* and extracted from the endosperms of locust bean seeds, respectively, show synergistic effect. The primary structure of xanthan consists of a cellulosic backbone substituted at C-3 on alternate glucose residues with a trisaccharide sidechain. The non-carbohydrate subchains include O-acetate on the inner mannose residue and pyruvate on the terminal mannose residue. XG forms a five-fold double helical structure and is soluble in water. Aqueous solutions of xanthan are thixotropic, but do not form hard gels [1]. LBG is a type of galactomannans composed of a $(1\rightarrow4)$ linked β-D-mannan backbone partially substituted at C-6 with α-D-galactosyl residues. Galactomannans are water-soluble and do not form gels [1]. A mixture of XG and galactomannan forms a thermoreversible gel at concentrations where each pure component does not form a gel.

The synergistic effect of XG and galactomannan would be attributed to intermolecular bindings between XG and galactomannan to form junction zones, but the structure of the junction zones has not been clarified [1]. In many cases, gelation of polysaccharides is accompanied by conformational transition of macromolecule. Vacuum-ultraviolet circular dichroism (VUVCD) is an effective tool for assignment of structures and conformational change of polysaccharides [2]. In a previous study, we measured VUVCD spectra of mixtures of XG and LBG [3]. A temperature dependent behavior of a CD peak at 200 nm due to a helical conformation of xanthan suggested the formation of a heterotypical double helix between XG and LBG [3, 4]. In this study, we performed preliminary VUVCD experiments for aqueous LBG solutions in order to measure a conformation change of LBG in the mixtures of XG and LBG and examine a concept of heterotypical helix formation in the future.

Two LBG samples with different molecular weights were used. One of the samples (LBG1) was purchased from Wako Pure Chemical Industries, Ltd., Japan ($M_v \sim 5 \times 10^5$), and the other (LBG2) was provided by CP Kelco Japan ApS ($M_v \sim 1 \times 10^6$). Galactose and mannose were purchased from Wako Pure Chemical Industries, Ltd., Japan. The VUVCD spectra of the mixture were measured from 260 nm to 170 nm under a nitrogen atmosphere by use of the VUVCD spectrophotometer constructed at Hiroshima Synchrotron Radiation Center (BL-12) and an assembled-type optical cell. The path length of the cell was adjusted with a Teflon spacer to 50 μm [2, 5].

Figure 1 shows the VUVCD spectra of aqueous solutions of LBG1 and LBG2. The molecular weight dependence of VUVCD spectra was not observed. In Figure 1, a spectrum calculated from the spectra of galactose and mannose solutions is also shown. There was a slight difference between the spectra of LBG and the calculated spectrum, which would be due to the effect of glycosidic linkages on the spectra of LBG.
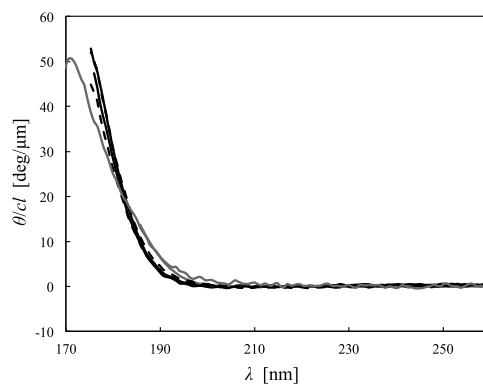
FIGURE 1. VUVCD spectra of 0.02 g/g solutions of LBG1 (solid line) and LBG2 (dashed line) and a spectrum calculated from VUVCD spectra of 0.2 g/g solutions of galactose and mannose (gray line).

REFERENCES

1. V. J. Morris, "Gelation of Polysaccharides" in Functional Properties of Food Macromolecules, 2nd edition, edited by S. E. Hill, D. A. Ledward and J. R. Mitchell, Gaithersburg: Aspen Publishers, Inc., 1998.
2. N. Ojima, K. Sakai, K. Matsuo, T. Matsui, T. Fukazawa, H. Namatame, M. Taniguchi and K. Gekko, Chem. Lett. 30, 522 (2001).
3. Y. Maki, K. Toriba, K. Ishizaka, K. Matsuo, HiSOR Activity Report 2015.
4. T. M. B. Bresolin, M. Milas, M. Rinaudo and J. L. M. S. Ganter, Int. J. Biol. Macromol. 23, 263 (1998).
5. K. Matsuo, K. Sakai, Y. Matsushima, T. Fukuyama and K. Gekko, Anal. Sci. 19, 129 (2003).

VUV-CD Measurements of Methylated Histone H3

Yudai Izumi[a] and Koichi Matsuo[a]

[a]*Hiroshima Synchrotron Radiation Center, Hiroshima University, Hiroshima 739-0046, Japan*

Keywords: Post-translational modification, Epigenetics

DNA wraps around core histone proteins composed of several subunits, named as H2A, H2B, H3, and H4, in eukaryotic nuclei. It has been revealed that the post-translational modifications, for example methylation, acetylation, phosphorylation, ubiquitination and so on, of histones play a substantial role in cellular functions [1]. Methylation of H3 proteins is one of the well-studied modifications and it is thought to be associated with either transcriptional activation or repression [1]. However, the conformations of methylated H3 proteins have not been revealed yet. Since the conformation of protein closely relates to its biological function, it is important to determine the structures of methylated H3 proteins in order to understand the cellular functions of methylated H3 proteins more precisely. In this work, we measured vacuum-ultraviolet circular dichroism (VUV-CD) spectra of lysine-9 mono-, di-, and trimethylated H3 and unmodified H3 proteins and predicted the secondary-structure sequences.

Recombinant *Xenopus laevis* unmodified and lysine-9 methylated H3 proteins were purchased from Merck Millipore and Acive Motif, respectively. Each reagent was dissolved with 25 mM sodium phosphate buffer supplemented with 250 mM sodium fluoride (pH 8.6 at 25°C). Final concentration of each histone solution was 1 mg/ml. CD spectroscopy was carried out in the BL12 beamline at the Hiroshima Synchrotron Radiation Center in Japan. Secondary structure contents of the samples were analyzed using VUV-CD spectra and SELCON3 program [2,3]. The secondary-structure sequences were predicted using neural-network method based on VUV-CD spectroscopic results [4].

Figure 1 shows VUV-CD spectra of unmodified and lysine-9 trimethylated H3 proteins. Unmodified H3 showed a positive peak around 190 nm and two negative peaks around 210 and 220 nm. These peaks are the characteristic CD peaks of α-helix structures. In contrast, trimethylated H3 showed only two negative peaks around 205 and 220 nm. Since CD spectral shapes reflect the secondary structure contents of proteins, the change in the VUV-CD spectrum of trimethylated H3 shows that the structural alterations of H3 were induced by trimethylation of lysine-9.

VUV-CD spectra of mono- and dimethylated H3 and secondary-structures sequences of all samples will be presented at the symposium.
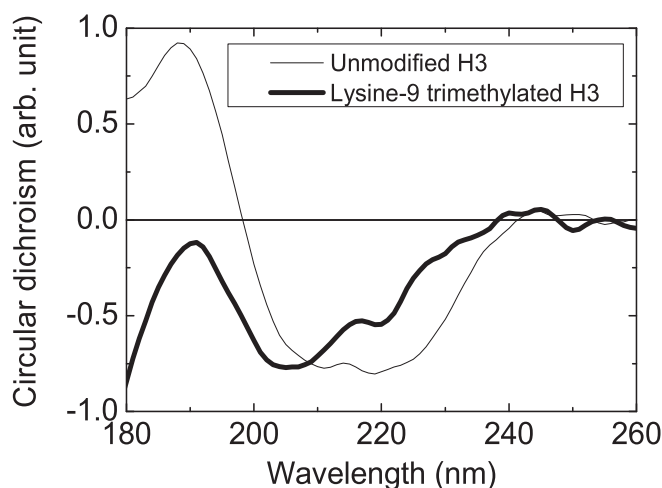
FIGURE 1. VUV-CD spectra of unmodified H3 (thin line) and lysine-9 trimethylated H3 (thick line).

REFERENCES

1. T. Kouzarides, *Cell* **128**, 693-705 (2007).
2. N. Sreerama *et al.*, *Protein Sci.* **8**, 370-380 (1999).
3. N. Sreerama and R. W. Woody, *Anal. Biochem.* **287**, 252-260 (2000).
4. K. Matsuo *et al.*, *Proteins* **73**, 104-112 (2008).

Studies on Structure and Amyloid Fibril Formation of α-Synuclein

Koichi Matsuo[a], Hanae Yamamoto[b], Seki Lee[b], Tomohiro Mizobata[b], Kunihiko Gekko[a], and Yasushi Kawata[b]

[a]Hiroshima Synchrotron Radiation Center, Hiroshima University, Higashi-Hiroshima, Hiroshima 739-0046, Japan
[b]Department of Chemistry and Biotechnology, Graduate School of Engineering, Tottori University, Tottori 680-8552, Japan

Keywords: Amyloid fibril, Secondary structures, α-Synuclein, VUVCD spectra

α-Synuclein is one of the causative proteins of familial Parkinson disease, which consists of 140 amino acid residues [1]. Its missense mutants, A30P [2], E46K [3], and A53T [4], have been observed in familial forms of early-onset Parkinson disease. α-Synuclein exists abundantly in a largely unfolded form in neuronal cells. Such a natively unfolded or intrinsically disordered protein is a hard target for X-ray crystallography and NMR spectroscopy, hence the structural details on the tertiary structure and amyloid fibrils of α-synuclein remain unclear. Circular dichroism (CD) spectroscopy is available for the secondary-structure analysis of both native and nonnative proteins under various solvent conditions; however, it does not provide detailed tertiary-structural information. CD spectra extended to the vacuum-ultraviolet (VUV) region below 190 nm (VUVCD spectroscopy) allows us to predict not only the secondary-structure contents but also the numbers and amino acid sequences of α-helix and β-strand segments, but such spectra have been previously unobtainable by conventional CD spectrometers. Here we have applied a synchrotron-radiation VUVCD spectroscopic method [5] for estimating the secondary structures of the wild-type (native form), three familial mutants, and amyloid fibrils of α-synuclein.

## 1. Secondary-Structure Analysis of α-Synuclein

VUVCD spectra of the wild-type and three mutants (A30P, E46K, and A53T) of α-synuclein were measured down to 178 nm in water at 25°C. As shown in Figure 1, the wild-type exhibited two negative peaks around 230 and 200 nm, suggesting a large amount of unordered structure. Two of the three mutants (A30P and E46K) showed similar spectra as that of the wild-type, but A53T α-synuclein showed a considerably different spectrum, suggesting a different secondary-structure composition to the other three proteins.
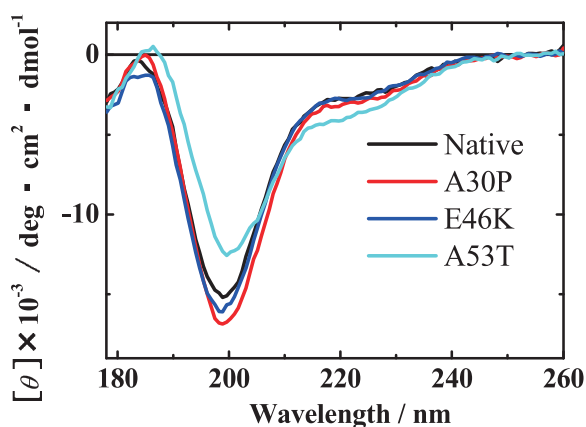
FIGURE 1. VUVCD spectra of wild-type and three mutants (A30P, E46K, and A53T) of α-synuclein in aqueous solution.

Next we estimated the contents and segments of the secondary structures of these proteins using a SELCON3 program. As shown in Figure 2, the wild-type, A30P, and E46K α-synucleins were composed of about 50% unordered structure, about 20% turn, and about 30% β-strand with 9–10 segments, but A53T contained a few percentage points of α-helix consisting of a single sequence segment. Also, most of the β-strands estimated may not form β-sheets but rather consist of partly unfolded conformations with distorted hydrogen bonds, as found in many denatured proteins. This disorder could conceivably lead to the initiation of amyloid fibril formation.
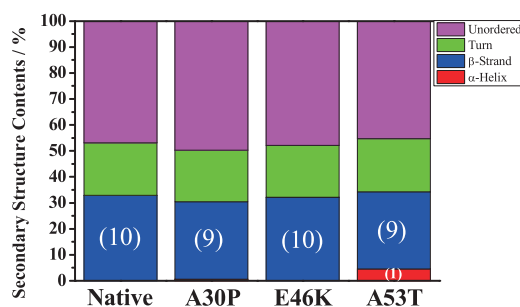

FIGURE 2. Histogram of secondary-structure contents of wild-type and three mutants (A30P, E46K, and A53T) of α-synuclein in aqueous solution. The numbers of α-helix and β-strand segments are shown in the parentheses.

2. VUVCD Measurements of Amyloid Fibrils

To study the structure of amyloid fibrils, VUVCD spectra of wild-type and three mutants of α-synuclein were measured after incubating their aqueous solutions for 450 hrs at 37°C, mixing once every few days. Interestingly, the VUVCD spectra of all of the α-synuclein proteins were almost the same as those in Figure 1, and no fibril formation was observed. This was also the case in experiments performed in aqueous 150 mM NaCl, with no significant change in the spectra being observed even after 600-hr incubation (Figure 3).

In contrast, the CD spectrum of the wild-type showed a negative peak around 220 nm, which is characteristic to amyloid fibril, after incubation with shaking in 25 mM Tris-HCl buffer (pH 7.4) containing 150 mM NaCl for 200 hrs at 37°C (data not shown). The VUVCD measurements of other three mutants under the same conditions are in progress in order to identify the effects of mutation on the fibril structure.
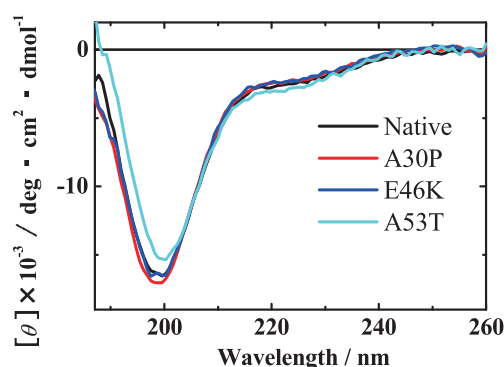
FIGURE 3. VUVCD spectra of wild-type and three mutants (A30P, E46K, and A53T) of α-synuclein in 150 mM NaCl solution.

REFERENCES

1. E. H. Norris et al., *Curr. Top. Dev. Biol.* **60**, 17–54 (2004)
2. R. Kruger et al., *Nat. Genet.* **18**, 106–108 (1998)
3. J. J. Zarranz et al., *Ann. Neurol.* **55**, 164–173 (2004)
4. M. H. Polymeropoulos et al., *Science* **276**, 2045–2047 (1997)
5. K. Matsuo and K. Gekko, *Methods in Mol. Biol.* **974**, 151–176 (2013)

Development of a Determination Method
for Absolute Configuration of Chiral Allenes
by Vacuum-Ultraviolet Circular Dichroism

Tatsuo Nehira[a], Yugo Tokunaga[a], Taiki Umezawa[b], and Koichi Matsuo[c]

[a]*Graduate School of Integrated Arts and Sciences, Hiroshima University,*
1-7-1 Kagamiyama, Higashi-Hiroshima 739-8521, Japan
[b]*Graduate School of Environmental Science, Hokkaido University, N10W5 Kita-ku Sapporo 060-0810, Japan*
[c]*Hiroshima Synchrotron Radiation Center, Hiroshima University,*
*2-313 Kagamiyama, Higashi-Hiroshima 739-0046, Japan*

Keywords: vacuum-ultraviolet electronic circular dichroism, ECD analysis, chiral allenes.

A series of omaezallene derivatives, newly discovered antifouling natural products [1], were synthetically prepared to complete their structure elucidation. Motivated with the fact that there is no versatile method for determining the absolute configurations of chiral allenes, except for a conventional method with optical rotations [2], we expect that our method [3] can be a powerful alternative.

$1: R_1 = H, R_2 = Br$
$2: R_1 = Br, R_2 = H$
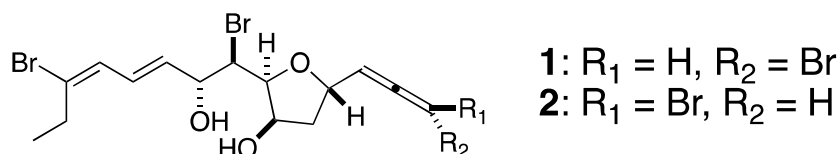
FIGURE 1. Structures of *ent*-omaezallene (**1**) and 1-*epi-ent*-omaezallene (**2**).

We adopted vacuum-ultraviolet electronic circular dichroism (VUV-ECD) [4] to observe ECD spectra down to 175 nm of synthetic intermediates **1** and **2** that were used in the previous study [1]. Since the calculated ECD spectra of **1** and **2** reproduced the experimental VUV-ECDs (**Fig. 2**), our method seems applicable to the chiral allenes in use. Further investigation with other chiral allenes is presently underway to generalize the method.
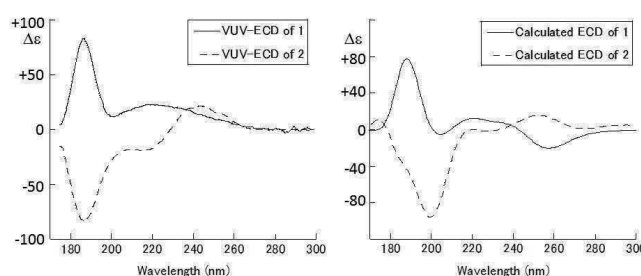
FIGURE 2. VUV-ECD spectra of **1** and **2** (left) along with their calculated ECD spectra (right).

REFERENCES

1. T. Umezawa, et al., *Angew. Chem. Int. Ed.* **2014**, *53*, 3909.
2. G. Lowe, *J. Chem. Soc. Chem. Commun.* **1965**, 411.
3. (a) T. Nehira, K. Matsuo, et. al, *Tetrahedron* **2015**, *71*, 6956. (b) H. Takekawa, K. Tanaka, E. Fukushi, K. Matsuo, T. Nehira, and M. Hashimoto, *J. Nat. Prod.* **2013**, *86*, 2503.
4. K. Gekko and K. Matsuo, *Chirality*, **2006**, *18*, 329.

Spectroscopic characterization of aromatic and nonaromatic monolayers by X-ray absorption spectroscopy

Shin-ichi Wada[a,b] and Atsunari Hiraya[a,b]

*aDepartment of Physical Science, Hiroshima University,
Higashi-Hiroshima 739-8526, Japan*
*bHiroshima Synchrotron Radiation Center, Hiroshima University,
Higashi-Hiroshima 739-0046, Japan*

Charge transfer dynamics at organic interfaces has attractive potential for future applications based on organic molecular devices. We consider that such dynamics can be evaluated by resonant core-excitations. Especially, site-selective ion desorption is a quite unique reaction after resonant core-electron excitation [1]. It is generally understood that selective ion desorption is promoted by the Coulomb repulsion between two holes at local bonding orbital(s) and the suppression of bonding power due to one electron at an anti-bonding orbital (so-called spectator Auger final states). This reaction can be obviously observed on solid surfaces, particularly well-ordered monolayers, like self-assembled monolayers (SAMs). This indicates the importance of the interaction between functional group at outermost surface (reaction center) and substrate [1].

On the other hand, core-hole clock (CHC) method is also powerful technique to measure ultrafast charge transfer dynamics. Generally, resonant Auger decay only occur after a resonant core excitation. But normal Auger electron can be also observed in solid surfaces. This is caused by fast dissipation of the excited electron to conductive band of the substrate before core-hole decay. So, we can get information about charge transfer dynamics from branching ratio between resonant Auger yield and normal Auger yield in comparison with the core-hole lifetime [2,3]. Actually, we have successfully measured the ultrafast charge transfer for aromatic molecular chain SAMs as strong reduction of resonant (spectator) Auger components in comparing with absorption intensity. And also we have confirmed that there is the critical relationship between site-selective ion desorption and ultrafast charge transfer dynamics [4]. Such charge transfer takes place along molecular orbitals of excited resonant states. That is to say, X-ray absorption spectra can also reflect the information about charge transfer dynamics and molecular conductivity. In this study, we studied X-ray absorption spectra of aromatic and nonaromatic monolayers based on the information about charge transfer dynamics clarified by the previous our studies.

Near edge X-ray absorption fine structure (NEXAFS) measurements were performed at the beamline BL-13 of HiSOR. During measurements, the experimental chamber had a base pressure of 1×10^{-8} Torr. NEXAFS spectra around the O K-edge were recorded in total electron yield (TEY) mode by measuring a sample drain current. SAMs were prepared by immersing Au substrates into 1.0 mM ethanol solutions of MHDA ($HS(CH_2)_{15}COOCH_3$), M2P ($HSPhPhCOOCH_3$), MP1 ($HSCH_2PhCOOCH_3$) and MP0 ($HSPhCOOCH_3$). All samples have $-COOCH_3$ at their head groups, connected by phenyl ring(s) with conductivity for MP0, MP1 and M2P SAMs, while MHDA has no conductivity due to insulating aliphatic methylene chain. Fig. 1 shows schematic drawings for SAMs used in this experiments together with PMMA ($[-CH_2C(CH_3)(COOCH_3)-]_n$) polymer thin film as a reference molecular system, which has a same $-COOCH_3$ moiety.

Fig. 2 shows the NEXAFS spectra in the O K-edge measured for PMMA thin film and MHDA SAM (insulating, nonaromatic system) and M2P, MP1 and MP0 SAMs (conductive, aromatic system). Assignments are also listed in the figure based on experimental and theoretical investigation [5]. Ionization potentials are estimated to be between 538 and 539 eV. Resonant peaks of $\sigma^*(O-CH_3) \leftarrow O(C-O)$ and $\sigma^*(C-OCH_3) \leftarrow O(C-O)$ exist at almost same energies in changing molecular systems, while two $\pi^*(C=O)$ peaks (from lower energy,

$\pi^*(C=O) \leftarrow O(C=O)$ and $\pi^*(C=O) \leftarrow O(C-O)$) shows red shift from non-aromatic to aromatic systems. Especially, energy shift of second π^* peaks is larger than the first ones. In compering two π^* resonances, second $\pi^*(C=O) \leftarrow O(C-O)$ resonances are attributed from intrinsic delocalization nature of π electrons around –COO-skeletons. So, further delocalization due to the bonding to the aromatic rings makes stabilization of π^* molecular orbitals around C=O moieties. This findings suggest that second $\pi^*(C=O) \leftarrow O(C-O)$ resonance can be good indicator of delocalization of π electrons, that is, molecular conductivity.

REFERENCES

1. S. Wada, H. Kizaki, Y. Matsumoto, R. Sumii and K. Tanaka, *J. Phys.: Condens. Matter* **18**, S1629-S1653 (2006).
2. J. Schnadt, P. A. Bruhwiler, L. Patthey, J. N. O'Sea, S. Sodergren, M. Odelius, R. Ahuja, O. Karis, M. Bassler, P. Persson, H. Siegbahn, S. Lunell, and N. Martensson, *Nature* **418**, 620-623 (2002).
3. A. Fohlische, P. Feulner, F. Hennies, A. Fink, D. Menzel, D. Sanchez-Portal, P.M. Echenique and W. Wurth, *Nature* **436**, 373-376 (2005).
4. S. Wada, M. Ogawa, S. Hosoda, R. Koga and A. Hiraya, *HiSOR Activity Report 2016*, 111-112 (2016).
5. O. Takahashi, K. Tabayashi, S. Wada, R. Sumii, K. Tanaka, M. Odelius and L.G.M. Pettersson, *J. Chem. Phys.* **124**, 124901(1-8) (2006).
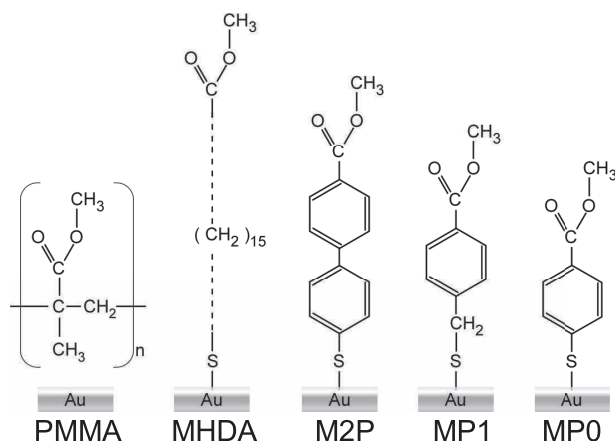
FIGURE 1. Molecular structure of SAMs used in this study, MHDA SAM (insulating), M2P, MP1, and MP0 SAMs (conductive) together with PMMA thin film as reference system.
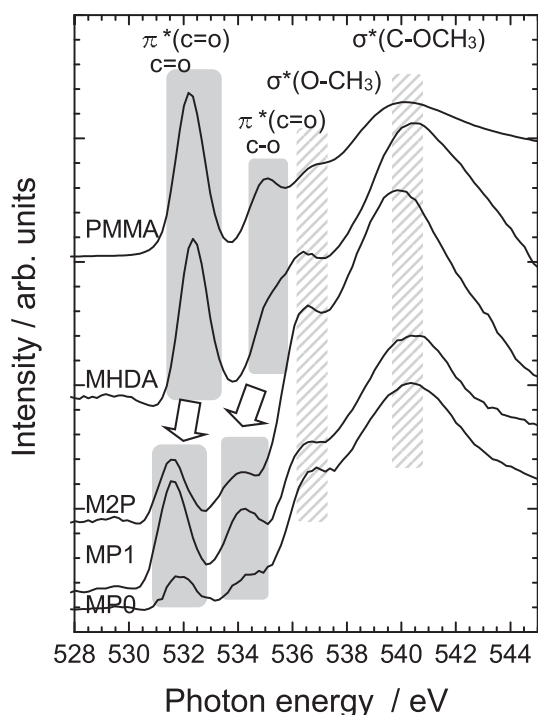
FIGURE 2. NEXAFS spectra in the O K-edge region measured for PMMA thin film and MHDA SAM (insulating, nonaromatic system) and M2P, MP1 and MP0 SAMs (conductive, aromatic system) with their assignments.

Characterization of gold nanoparticles synthesized by pulsed laser ablation in liquids

Shin-ichi Wada[a,b], Akira Himeda[a] and Atsunari Hiraya[a,b]

[a]*Department of Physical Science, Hiroshima University,*
Higashi-Hiroshima 739-8526, Japan
[b]*Hiroshima Synchrotron Radiation Center, Hiroshima University,*
*Higashi-Hiroshima 739-0046, Japan*

Keywords: Gold nanoparticles, Pulsed laser ablation in liquid (PLAL), X-ray photoelectron spectroscopy (XPS)

Metal nanoparticles have the great potential on material and functional properties differently from the bulk states, because of large surface area and different electronic states of nanoparticles. Gold nanoparticles is also one of such promising nanomaterials, which possess high catalytic activity in several nanometer scale although gold is quite stable in the bulk state. Gold nanoparticles are usually synthesized by chemical redox methods using tetrachloroauric acid ($HAuCl_4$). Reducing and/or protecting agents needed in the synthesis processes have role to control nanoparticle size and prevent aggregation/sedimentation by covering gold nanoparticles by the agents.

Recent research progress of gold nanoparticles also opens new frontiers in assembly of nanoparticles which embody new function unlike the solo particles. We have started to synthesize one dimensionally assembled gold nanoparticles in order to apply to nano-order conductive devise and analytical or bio sensors based on patterned nanoparticle array. For this purpose, we have also performed the synthesis of naked gold nanoparticles by means of pulsed laser ablation in liquid (PLAL) method. In this study, gold nanoparticles synthesized by laser ablation in water and ethanol was evaluated by X-ray photoelectron spectroscopy (XPS) as well as scanning electron microscopy (SEM) and visible absorption spectroscopy.

Fig. 1(a) schematically depicts synthesis method of gold nanoparticles by PLAL. Laser pulse (Spectra Physics Empower; 527 nm, repetition rate 1 kHz, pulse duration ~200 ns, pulse energy 10 mJ/pulse) was focused by f=200 lens and irradiate onto a gold plate in water (Milli-Q) or ethanol (Kanto Chemical; 99.5%). Liquid level was kept at 1 cm above the gold surface to form plasma condition effectively synthesize uniform nanoparticles (Fig. 1(b)). Position of the gold plate was periodically changed to prevent deep etching on the same local place. SEM measurements were carried out by using a field emission SEM (FE-SEM; Hitachi High-Technologies S-5200) of Natural Science Center for Basic Research and Development in Hiroshima University. From the SEM images, we could easily check the size and shape of gold nanoparticles. On the other hand, visible absorption measurements allow us to evaluate concentration of nanoparticles in colloidal phase. XPS measurements were performed at BL13 of HiSOR to evaluate surface property of nanoparticles.

Fig. 2 shows typical SEM results of gold nanoparticles synthesized by pulsed laser ablation in (a) water and (b)
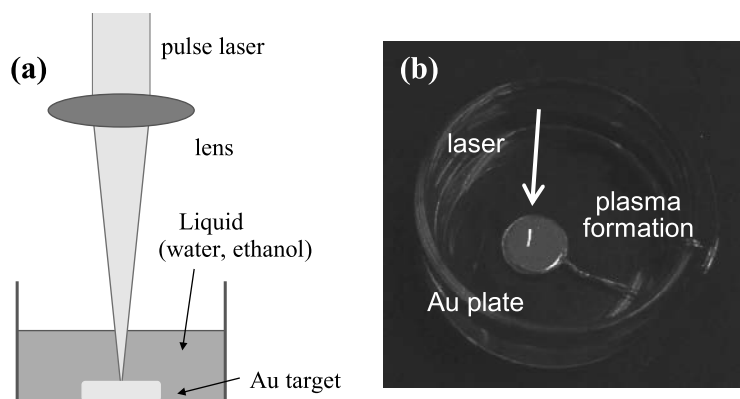

FIGURE 1. (a) Schematic drawing of synthesis of gold nanoparticles by PLAL method. (b) Snapshot of laser irradiation onto a gold plate, showing the formation of plasma along the laser irradiation.

ethanol during several hours. The images indicate successful synthesis of uniform gold nanoparticles with about 10 nm diameter in both liquids. Visible absorption measurements can also evaluate synthesis of nanoparticles as a typical absorption band around 520 nm due to surface plasmon resonance of gold nanoparticles. Moreover, Fig. 3 can estimate the concentration of colloidal condition of nanoparticles from absorption intensity, indicating to be 1.7×10^{11} particles/mL (= OD 0.0029 / ε 1.01×10^{8} $M^{-1}cm^{-1}$ / d 1 mm). Fig. 4 shows XPS spectra measured around Au 4f region. Binding energy was calibrated by the bulk Au 4f 7/2 peak at 84.0 eV. The spectra indicate apparent energy shift of nanoparticles. This lower energy shift with 0.8 eV of nanoparticles is caused by screening of core-level 4f electrons due to charging on surface levels of gold nanoparticles, suggesting that naked gold nanoparticles synthesized PLAL charge negatively on their surfaces and therefore, even naked nanoparticles can keep stability in liquid without any protection materials.
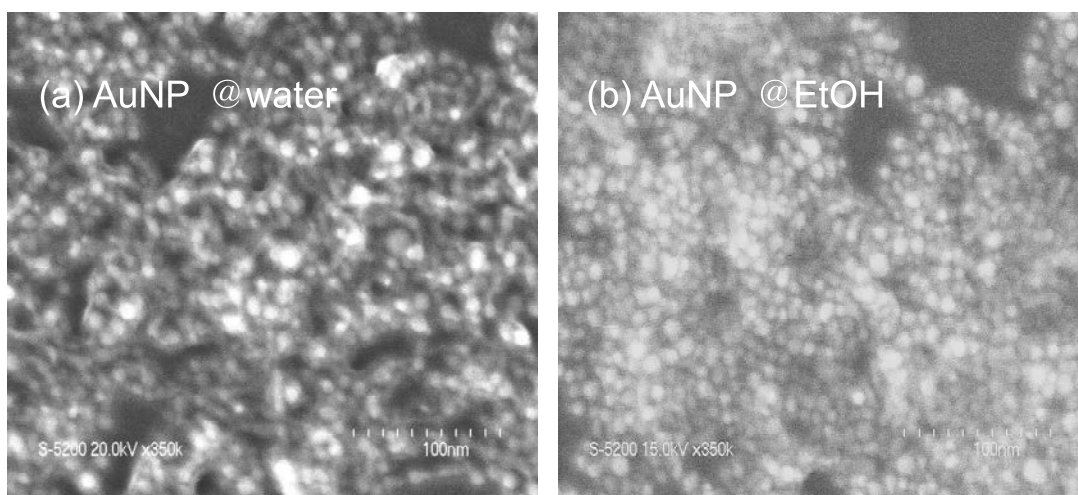
FIGURE 2. SEM images of gold nanoparticles synthesized by pulsed laser ablation in (a) water and (b) ethanol.
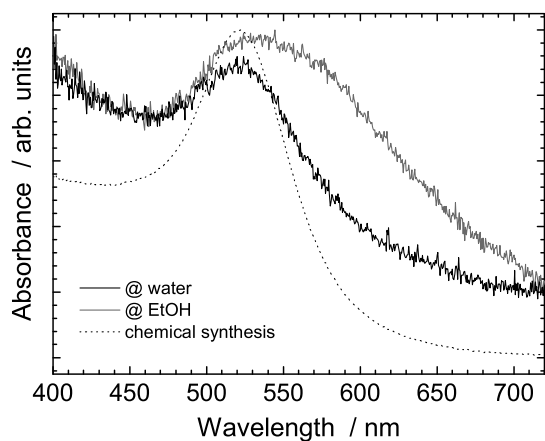
FIGURE 3. Visible absorption spectra of gold nanoparticles synthesized by PLALA in water and ethanol together with nanoparticles by chemical redox methods (purchased).
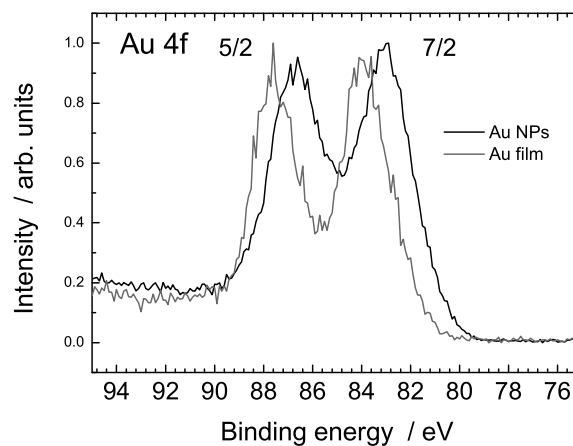
FIGURE 4. XPS spectra measured for gold nanoparticles and films on n-type Si(100) substrates.

Feasibility study for soft X-ray absorption experiments at ambient pressure or low vacuum at HiSOR-BL14

Kazuki Ishii[a], Masahiro Sawada[b], Hirofumi Namatame[b]

[a]*Department of Physical Science, Graduate School of Science, Hiroshima University,*
1-3-1 Kagamiyama, Higashi-Hiroshima, 739-8526, Japan
[b]*Hiroshima Synchrotron Radiation Center, Hiroshima University,*
2-313 Kagamiyama, Higashi-Hiroshima, 739-0046, Japan

Keywords: soft X-ray absorption spectroscopy; ambient pressure condition; fluorescent yield; resonant soft x-ray reflectivity

Soft X-ray absorption spectroscopy and the rerated dichroic measurements are powerful technique to probe chemical states (oxidation or valence states), electronic states orbital and magnetic states of matters. At HiSOR-BL14[1, 2], so far, soft X-ray absorption spectroscopy (XAS), soft X-ray linear dichroism (XLD) and soft X-ray magnetic circular dichroism (XMCD) have been actively utilized for many types of crystallized compounds, surface structures and nanomaterials, especially composed of transition metals including magnetic elements. In the absorption measurements, total electron yield (TEY) method has been adopted as measurement technique of absorption intensities instead of transmittance measurement. TEY method is a simple and effective way to obtain relative absorption intensities for non-transparent materials, but the probing depth is limited to several nanometers from sample surfaces because of short escape depth of emitted electrons. The surface sensitivity of TEY method requires proper surface preparations and an ultra-high vacuum (UHV) condition, whose difficulties narrow down the scope of target materials and make strict limitations on environment field control experiments such as operando experiments. Once we can separate UHV sections of the beamline from a measurement chamber with keeping adequate transmission of soft X-ray, photon-in-photon-out measurement is a straight solution to achieve soft X-ray absorption experiments at ambient pressure or low vacuum.

To investigate feasibility of the experiments under ambient/low-vacuum condition at HiSOR-BL14, we have examined a vacuum separation technique, a possibility of using fluorescent yield method in the absorption spectroscopy and a compatibility between beamline optics and resonant reflectivity measurements whose magnetic dichroism (MRXR) yields similar information to XMCD measurement. We have tested vacuum separation by a SiN window with 200 nm thickness membrane whose size is 3mm × 3mm, and have confirmed the window achieves so low leak-rate as to separate between an UHV section and ambient pressure, with good X-ray transmission (approximately 85% @ 850eV). Using the SiN window practically at an end-station of HiSOR-BL14, we have successfully carried out fluorescence measurement with a recent type of silicon drift detector (SDD) without UHV condition. We have found XAS measurements with fluorescent yield method is acceptable from a practical standpoint as long as the accumulation time is adequate. From a lay-trace simulation based on realistic optical parameters of the beamline, we have confirmed reflectivity measurements are operable with incident angle accuracy of 4.5 mrad along vertical direction.

REFERENCES

1. M. Sawada, K. Yaji, M. Nagira, A. Kimura, H. Namatame, M. Taniguchi, AIP Conf. Proc. **879**, 551 (2007).
2. M. Sawada, T. Ueno, T. Tagashira, H. Namatame, M. Taniguchi, AIP Conf. Proc. **1234**, 939 (2010).

Study of Interlayer Magnetic Coupling of Co/h-BN/Ni(111) by Soft X-ray Magnetic Circular Dichroism

Norikazu Ichikawa[a], Kazuki Ishii[b], Masahiro Sawada[c],
Akio Kimura[b], Hirofumi Namatame[c]

[a]*Department of Physical Science, Faculty of Science, Hiroshima University,
1-3-1 Kagamiyama, Higashi-Hiroshima, 739-8526, Japan*
[b]*Department of Physical Science, Graduate School of Science, Hiroshima University,
1-3-1 Kagamiyama, Higashi-Hiroshima, 739-8526, Japan*
[c]*Hiroshima Synchrotron Radiation Center, Hiroshima University,
2-313 Kagamiyama, Higashi-Hiroshima, 739-0046, Japan*

Keywords: boron nitride, cobalt, nickel; X-ray magnetic circular dichroism

TMR (tunnel magnetoresistance) effect is one of key phenomena for developing of spintronic devices, whose effect is observed in multilayer structures consist of a set of ferromagnetic (FM) electrode layers and an insulator layer sandwiched by them. Since the magnetoresistance is dependent on the relative spin alignment between the both of FM electrode layers, it is essentially important to investigate inter-layer magnetic coupling and interface magnetism at interfaces contacted with the insulator barrier layer. TMR structures with an insulator monolayer of hexagonal boron nitride (h-BN) is regarded as one of candidates for ideal TMR device, where a pinhole-less ultrathin barrier layer ensures high performance (large MR ratio) and good reliability which are compatible with low power consumption. Actually, some studies have been reported on spin-dependent transport properties in realistic TMR structures with a monolayer h-BN [1, 2], showing the MR ratio up to 150% at room temperature. To clarify magnetic state at the interface between a magnetic layer and monolayer h-BN, we have investigated magnetic properties of Co layers in Co/h-BN/Ni(111) structure by means of soft X-ray magnetic circular dichroism (XMCD) spectroscopy.

We fabricated Co/h-BN/Ni(111) films for the thickness dependence measurements of XMCD spectra, where the Co ultrathin films had wedge-type structures. High-quality h-BN was prepared on Ni(111) surface by cracking of vaporized borazine ($B_3N_3H_6$) [3]. The samples of Co/h-BN/Ni(111) are obtained by MBE evaporation of Co at room temperature. The XMCD experiments were performed just after the sample preparations *in-situ* at HiSOR-BL14 [4, 5]. From analysis of the thickness-dependent spectra measured in normal incidence geometry with magnetic field of 1.1 T along sample normal direction, antiferromagnetic (AFM) coupling between Co and Ni(111) substrate has been clearly observed. The AFM coupling is getting weaker with the Co thickness increased. The XMCD signal of Co whose sign is opposite to Ni, disappears at 6.6 ML.

REFERENCES

1. A. Dankert, M. V. Kamalakar, A. Wajid, R. S. Patel, and S. P. Dash, Nano. Res. **8**, 1357 (2015).
2. M. Piquemal-Banci, R. Galceran, S. Caneva, M. -B. Martin, R. S. Weatherup, P. R. Kidambi, K. Bouzehouane, S. Xavier, A. Anane, F. Petroff, A. Fert, J. Robertson, S. Hofmann, B. Dlubak, and P. Seneor, Appl. Phys. Lett. **108**, 102404 (2016).
3. C. Oshima and A. Nagashima, J. Phys.: Condens. Matter **9**, 1 (1997).
4. M. Sawada, K. Yaji, M. Nagira, A. Kimura, H. Namatame, M. Taniguchi, AIP Conf. Proc. **879**, 551 (2007).
5. M. Sawada, T. Ueno, T. Tagashira, H. Namatame, M. Taniguchi, AIP Conf. Proc. **1234**, 939 (2010).

Magnetic anisotropy of Fe/Pd(001) bilayer dependent on Pd film thickness

Shota Nakahara[a], Shunsuke Sakuragi[a], Kousuke Mochihara[a], Masahiro Sawada[b] and Tetsuya sato[a]

[a] Department of Applied Physics and Physico-Informatics, Faculty of Science and Technology, Keio University, 3-14-1 Hiyoshi, Yokohama kohoku-ku, 223-8522 Japan
[b]Hiroshima Synchrotron Radiation Center, Hiroshima University, 2-313 Kagamiyama, Higashi-Hiroshima, 739-0046 Japan

Keywords: Magnetic anisotropy, Thin film, Quantum well, Fe, Pd.

FePt and FePd ordered alloys with $L1_0$ structure exhibit large uniaxial magnetic anisotropy and they can be used for high-density magnetic storages. To design future magnetic storage, the origin of magnetic anisotropy should be understood in detail based on the electronic state.

In our recent research, Pd(001) thin film periodically showed ferromagnetism dependent on film thickness [1]. This has been explained based on the quantum-well (QW) states, which appear in a nanoscale thin film. When the flat band, which originates from the QW state, approaches to Fermi energy, the ferromagnetism appears. In this research, the system in which Fe layers are deposited on Pd thin film is used. This is because the anisotropy of pseudo $L1_0$ FePd, formed at the Fe/Pd interface, should systematically change dependent on the Pd thickness through the modulation of electronic states.

We grew epitaxial Pd thin film on $SrTiO_3$(001) (STO) substrate in an ultra-high vacuum by three-step method [2]. Two mono-layers (MLs) of Fe were deposited on Pd/STO in the other deposition apparatus. Additional deposition of 20 nm of Au was performed to prevent the oxidation of Fe layer. The magnetization measurement of Pd/STO(001) and Au/Fe/Pd/ STO(001) was performed by a superconducting quantum interference device (SQUID) magnetometer at 300 K in in-plane and out-of-plane magnetic field.

We measured x-ray magnetic circular dichroism (XMCD) spectra of epitaxially grew non capped (1.2 ML)Fe/(1.0 - 3.8 nm)Pd/Cu(001) without expose to the air at HiSOR BL-14. In this measurement, Fe signal was selectively measured at Fe L edge at room temperature in a magnetic field applied out-of-plane magnetic field.

Magnetic anisotropy energy (MAE) in this research is calculated by the following relation,

$$\text{MAE} = \int (m_{\text{out}} - m_{\text{in}}) \mathrm{d}H \,, \tag{1}$$

where m_{out} and m_{in} are the out-of-plane and in-plane magnetic moment per sample area. All the samples of Au/Fe/Pd(001) have in-plane magnetic anisotropy. Figure 1 shows the MAE/($m_{\text{S(FePd)}}$ - $m_{\text{S(Pd)}}$) as a function of Pd thickness.

Figure 2 shows the Fe L3 XMCD intensity, the Pd M3 x-ray absorption spectroscopy (XAS) intensity, and the ratio of Fe spin magnetic moment (mspin) and orbital magnetic moment (morb) as a function of Pd thickness.
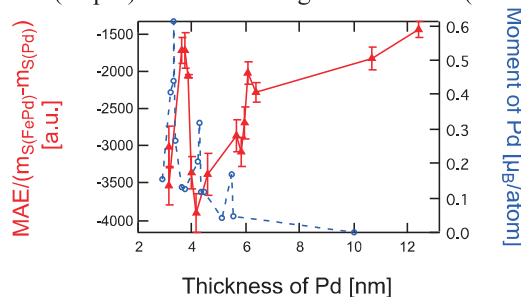
FIGURE 1. Pd thickness dependence of MAE of Fe/Pd divided by ($m_{\text{S(FePd)}}$ - $m_{\text{S(Pd)}}$) (red). Blue points show the magnetic moment of Pd(001).
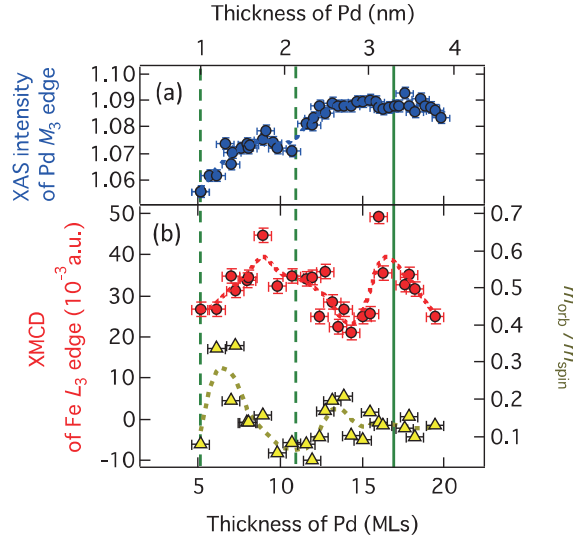
FIGURE 2. The XAS intensity of Pd (a, blue), XMCD intensity of Fe (b, red circle), and the ratio of mspin and morb (b, yellow triangle) as a function of Pd thickness. Green line shows the Pd film thickness at which Pd moment shows maximum in Fig. 2. Green dashed lines show the Pd film thickness expected to have maximum moment of Pd from Fig. 2.

In order to calculate the magnetic anisotropy energy of Fe per volume, it is necessary to estimate the film thickness of Fe. Provided that the change in magnetic moment at interface is negligible, magnetic moment of Fe can be approximately obtained by ($m_{S(FePd)}$ - $m_{S(Pd)}$). Thus, MAE/($m_{S(FePd)}$ - $m_{S(Pd)}$) can be regarded to magnetic anisotropy energy per volume, because the thickness of Fe is proportional to the magnetic moment of Fe. As shown in Fig. 1(b), the MAE/ ($m_{S(FePd)}$ - $m_{S(Pd)}$) becomes the minimum at the film thickness at which Pd has peak of magnetic moment. Considering the fact that QW band of Pd locates at Fermi energy at this thickness, in-plane magnetic anisotropy energy of Fe increases at the thickness of Pd at which Pd QW bands locate at the Fermi energy.

As shown in Fig. 2, m_{orb}/m_{spin} decreases near the Pd film thicknesses as shown by the green solid and dashed lines where the Pd magnetic moment shows peak and MAE/($m_{S(FePd)}$ - $m_{S(Pd)}$) has a minimum. This indicates that the morb decreases when magnetic anisotropy energy of Fe increases. Such a correlation between m_{orb} and magnetic anisotropy is consistent with the previous theoretical calculation [3]. In Fig.2, in addition, XAS intensity shows dips near the Pd film thicknesses shown by the green solid and dashed lines. This reflects the change in electronic structure of Pd to correlate with the change in magnetic anisotropy of Fe, because the XAS intensity corresponds to the hole number in Pd.

The magnetic anisotropy of Fe/Pd system has been understood based on the spin-orbit coupling (SOC) between $4d_{xz,yz}$ occupied (unoccupied) band of Pd and the unoccupied (occupied) band of Fe near Fermi energy [4]. Considering that the QW band is composed by $4d_{xz,yz}$ orbitals near Fermi energy in Pd(001) ultrathin film [5], the Pd thickness dependent change in the QW band consisting of $4d_{xz,yz}$ bands modulates the SOC to induce the observed change in magnetic anisotropy of Fe.

REFERENCES

1. S. Sakuragi, T. Sakai, S. Urata, S. Aihara, A. Shinto, H. Kageshima, M. Sawada, H. Namatame, M. Taniguchi, and T. Sato, *Phys. Rev. B* **90**, 054411 (2014).
2. T. Wagner, G. Richter, and M. Rühle, *J. Appl. Phys.* **89**, 2606-2612 (2001).
3. P. Bruno, *Phys. Rev. B* **39**, 865-868 (1989).
4. D.-S. Wang, R. Wu, and A. J. Freeman, *Phys. Rev. B* **47**, 14932-14947 (1993).
5. S. Aihara, H. Kageshima, T. Sakai, and T. Sato, *J. Appl. Phys.* **112**, 073910 (2012).

Ferromagnetism, cerium valence, and heavy fermions in Ce(Co$_{1-x}$Cu$_x$)$_5$: an XAS study

Tetsuro Ueno[a,b,c], Kotaro Saito[b,c], Hiroaki Shishido[d,e], Munehisa Matsumoto[b,f], and Masahiro Sawada[g]

[a]Quantum Beam Science Research Directorate, National Institutes for Quantum and
Radiological Science and Technology, 1-1-1 Koto, Sayo 679-5148, Japan
[b]Elements Strategy Initiative Center for Materials Science, National Institute for Materials Science,
1-2-1 Sengen, Tsukuba 305-0047, Japan
[c]Institute of Materials Structure Science, High Energy Accelerator Research Organization,
1-1 Oho, Tsukuba 305-0801, Japan
[d]Department of Physics and Electronics, Osaka Prefecture University, 1-1 Gakuen-cho, Naka-ku,
Sakai 599-8531, Japan
[e]NanoSquare Research Institute, Osaka Prefecture University, 1-1 Gakuen-cho, Naka-ku,
Sakai, 599-8531, Japan
[f]Institute for Solid State Physics, The University of Tokyo, 5-1-5 Kashiwanoha, Kashiwa 277-8581, Japan
[g]Hiroshima Synchrotron Radiation Center, Hiroshima University, 2-313 Kagamiyama,
Higashihiroshima 739-0046, Japan

We address combined trends of magnetism and $4f$-electron localization/delocalization in a $4f$-$3d$ intermetallic compound, Ce(Co$_{1-x}$Cu$_x$)$_5$ with $0.3 \leqq x \leqq 0.8$. Spin-orbit interaction couples the low-energy physics in the spin/orbital sector and relatively high-energy physics in the charge sector, paving a way to possibly exploiting the physics of valence fluctuations in designing the intrinsic magnetism on demand. The motivations for the particular materials series Ce(Co,Cu)$_5$ in our study are twofold: 1) RCo$_5$ (R = rare earth) makes a prototype which makes a building block of rare-earth permanent magnet compounds [1] in the context of practical applications. 2) on the fundamental point of view, CeCu$_5$ is one of the typical magnetic Kondo lattices [2] whose Sommerfeld coefficient can be enhanced to challenge the heavy-fermion compound CeCu$_6$ once Cu is slightly alloyed with Co. The composition parameter x controls the overall trend between $4f$-electron antiferromagnetism in a Kondo lattice and $3d$-electron ferromagnetism, together with the valence transition of Ce from a mixed-valence regime in $x < 0.4$ to a trivalent regime in $x > 0.6$. We mainly report the results of our temperature-controlled X-ray absorption spectroscopy (XAS) measurements.

Ce(Co$_{1-x}$Cu$_x$)$_5$ ($0.3 \leqq x \leqq 0.8$) polycrystals were grown by arc-melting. XAS experiment was performed at HiSOR BL-14, Hiroshima University, Japan. Clean surface of the sample was prepared by filing in ultra-high vacuum. X-ray absorption spectra were collected by total electron yield method measuring the sample drain current. Photon energy was tuned to Ce $M_{4,5}$ absorption edges ($3d$-$4f$ transition) which we can directly probe $4f$ electrons of cerium.

X-ray absorption spectra are shown in Fig. 1 as a function of temperature (T) and Cu concentration (x). At the lowest temperature in our measurement which is 20K, we observe a clear trend of the valence transition near the ground state of Ce(Co$_{1-x}$Cu$_x$)$_5$, from a mixed valence state in $x \leqq 0.5$ and the trivalent state for $x \geqq 0.6$ as seen in Fig. 1(a). The mixed-valence state is almost temperature independent for $x = 0.3$ and $x = 0.4$ while in the Cu-rich sample in the room-temperature measurement the well localized nature of $4f$-electrons can be seen in the absence of $(4f)^0$ satellite peak.
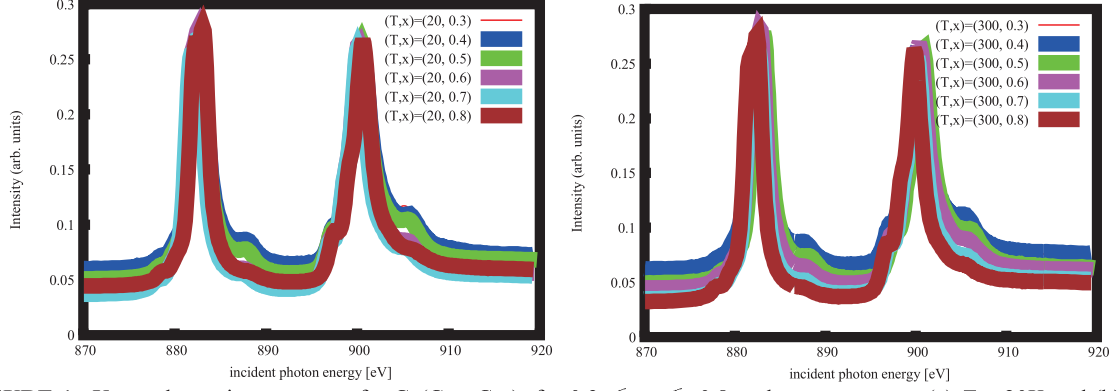
FIGURE 1. X-ray absorption spectrum for $Ce(Co_{1-x}Cu_x)_5$ for $0.3 \leqq x \leqq 0.8$ at the temperatures (a) $T = 20K$ and (b) $T = 300K$. In plotting the data, peak heights coming from the $(4f)^1$ state have been adjusted to match onto each other so that the trends in the satellite peak coming from $(4f)^0$ can be elucidated. Overall, increasing Cu concentration x suppresses the $(4f)^0$ contribution. Valence transition is most clearly seen at the lowest temperature in our measurement at 20K.

    $CeCo_5$ at $x = 0$ features $3d$-electron ferromagnetism while $CeCu_5$ at $x = 1$ features $4f$-electron antiferromagnetism. Starting at $x = 1$, Doniach's picture [3] concerning the competition between a phase with magnetic long-range order and Kondo-screened phase may provide a starting point to understand the trends among magnetism and heavy-fermion behavior in cerium-based intermetallic compounds [4]. Magnetism can be realized by Ruderman-Kittel-Kasuya-Yosida (RKKY) interaction of which scale is parametrized by $N_F J_K^2 N(0)$, where J_K is the Kondo coupling, N_F is an effective degeneracy of the local f-electron state, and $N(0)$ is the density of states on the Fermi level, while the Kondo effect of which scale is characterized by $D \, exp\{-1/[N_F J_K N(0)]\}$, where D is the effective bandwidth, can screen out the localized f-electron magnetic moments. The polynomial growth with respect to J_K of the former wins over the exponential dependence for small $J_K N(0)$ while Kondo effect can dominate for large $J_K N(0)$. Indeed, a realistic Kondo-lattice simulation of $CeCu_5$ reveals that this particular material lies on the $4f$-electron antiferromagnetic phase and alloying with Co would drive the material toward a magnetic quantum critical point (QCP) as long as $4f$-electrons therein remain localized and d-electron conduction band remain to sit on the verge of magnetic polarization. These situations seem to hold for $1 \geqq x \geqq 0.6$ [5]. Non-trivial temperature dependence in the cerium valence state combined with the possible interplay between $3d$-electron ferromagnetism and $4f$-electron antiferromagnetism could be detected near the possible QCP, which unfortunately dropped out of our measurement plan in the fiscal year 2016, where we invested our measurement time intensively on both of the Cu-rich side and Co-rich side. Focus measurement on QCP region will be separately planned.

    Good temperature control implemented at HiSOR BL-14 has helped us to investigate the valence state of Ce in $Ce(Co,Cu)_5$ which is taken as an archetypical compound to extract the essential physics in the intrinsic magnetism of rare-earth permanent magnet compounds. For the Co-rich compounds which represents a typical composition in permanent magnets, mixed-valence state of Ce is dominant from the room temperature down to 20K. Being in the proximity to the valence transition in the composition space could help in getting useful magnetic properties, which we have confirmed in separate bulk measurements [6]. Combining those bulk measurements and the present microscopic probing of the intrinsic electronic structure, we hope to get an insight toward a principle for designing useful magnet compounds.

    Helpful comments given by Yoshio Kuramoto and discussions with Julie B. Staunton in related projects are gratefully acknowledged. The present research has been supported by JSPS KAKENHI grant 15K13525.

REFERENCES

1. for a review, see H.-S. Li and J. M. D. Coey, *Handbook of Magnetic Materials Vol. 6*, Ed. K. H. J. Buschow, Elsevier Science Publishers B. V., 1991, pp. 1-83.
2. for a review, see E. Bauer, *Adv. Phys.* **40**, 417-534 (1991).
3. S. Doniach, Physica **91B** 231-234 (1977).
4. trend in magnetism and heavy-fermion in Ce-115 compounds was addressed in M. Matsumoto *et al.*, Phys. Rev. B **82**, 180515 (2010).
5. H. Shishido, M. Matsumoto, T. Ueno, and K. Saito, talk in the 71st JPS annual meeting, 21pBL-16, Tohoku Gakuin Univ. (2016).
6. H. Shishido *et al.* in preparation.

Magnetic property of chemically exfoliated manganese oxide nanosheet

Y. Naruo[a], K. Takaki[a], M. Sawada[b], H. Namatame[b], M. Taniguchi[b],
A. Funatsu[c], M. Hara[c]

[a]*Graduate School of Science and Technology, Kumamoto University,*
2-39-1 Kurokami, Kumamoto 860-8555, Japan
[b]*Hiroshima Synchrotron Radiation Center, Hiroshima University,*
2-313 Kagamiyama, Higashi-Hiroshima 739-0046, Japan
[c]*Faculty of Advanced Science and Technology, Kumamoto University,*
2-39-1 Kurokami, Kumamoto 860-8555, Japan

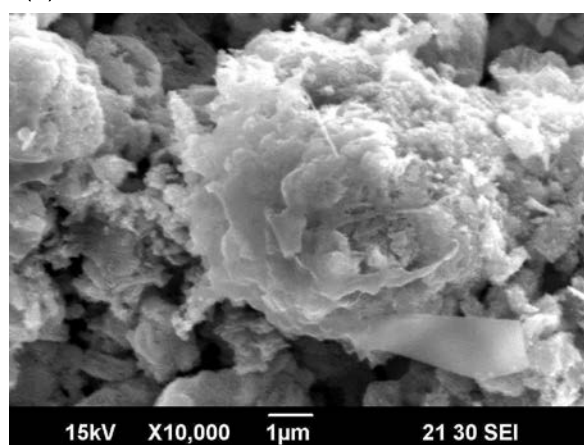**Keywords:** manganese oxide, nanosheet, XAS, XMCD

Two-dimensional (2D) materials have attracted great interests not only in fundamental physics but also in applied physics. Atomically thin graphene is the most representative 2D material for various applications. Graphene has a long spin diffusion length and plays an important role in future 2D spintronics devices [1]. However, there is no intrinsic spontaneous magnetization in graphene excluding a small contribution near zigzag edges [2].   Studies of 2D magnetic materials are essential to achieve future spintronics devices based on 2D materials. We have recently reported magnetic behavior of chemically exfoliated Mn-doped titanium oxide nanosheet [3]. In the present work, we investigate magnetic property of manganese oxide nanosheet by X-ray magnetic circular dichroism (XMCD) measurement.

We firstly prepared starting layered manganese oxide and then obtained a protonic form of the layered manganese oxide in an HCl solution. Figure 1 shows scanning electron microscopy (SEM) images of the starting layered oxides $K_{0.45}MnO_2$ and their protonated oxides $H_{0.13}MnO_2$. The protonic-layered crystals were exfoliated into single-layer manganese oxide nanosheets in a tetrabutylammonium hydroxide (TBAOH) solution [4]. Finally, the nanosheets were deposited on a heavily doped Si substrate by the Langmuir-Blodgett (LB) technique.
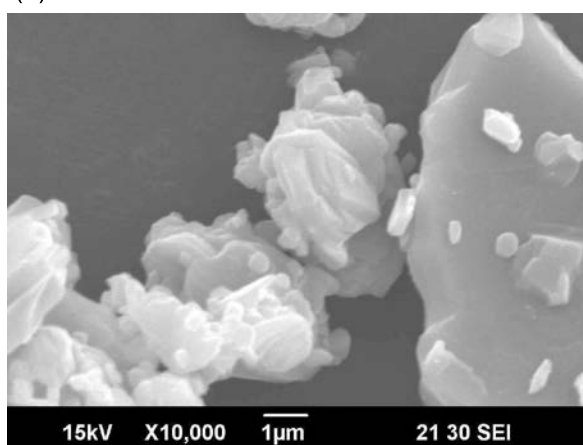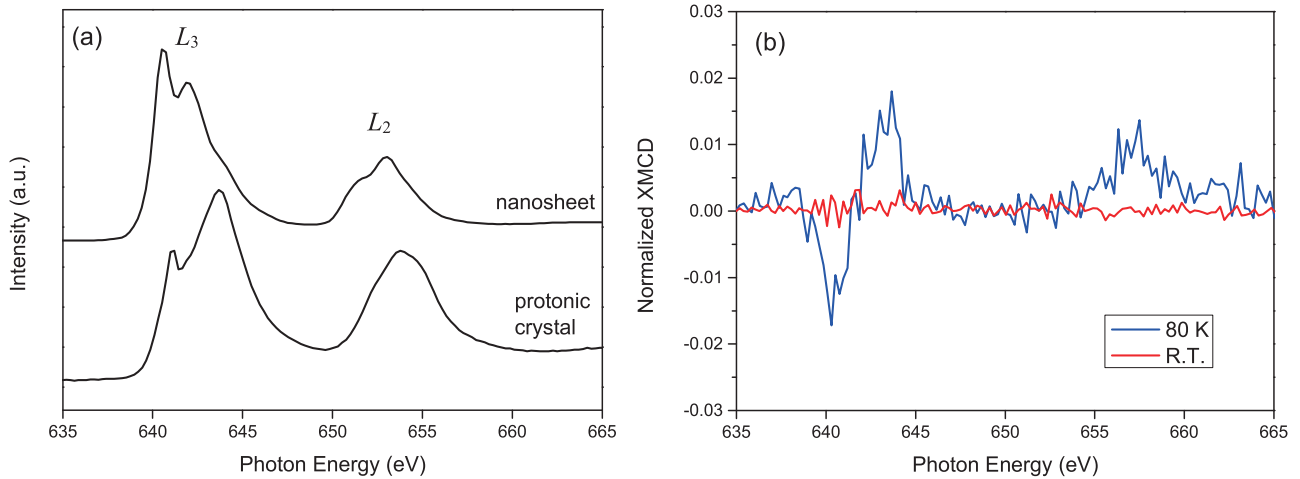
(a)   (b)

FIGURE 1. SEM images of (a) $K_{0.45}MnO_2$ and (b) $H_{0.13}MnO_2$.

FIGURE 2. (a) XAS spectra for the protonic crystals and the exfoliated manganese oxide nanosheets. (b) Normalized XMCD spectra for the nanosheets at room temperature (R. T.) and at 80 K.

Soft X-ray absorption spectroscopy (XAS) experiments were carried out at BL-14 beam line of HiSOR. The spectra were taken in total electron yield mode by measuring the drain current through the Si substrate. Figure 2(a) shows Mn XAS spectra for the protonic crystals and the exfoliated nanosheets. There is a significant difference in the XAS spectra, which indicates a change in the electronic configuration of 3d states in Mn atoms during the exfoliation process in the TBAOH solution or the deposition process on the Si substrate.

XMCD spectra were obtained from the XAS spectra by changing the polarity of external magnetic field (B = 1.1 T) perpendicular to the sample. The XMCD spectra ($\mu^+ - \mu^-$) in Fig. 2(b) are normalized by the value of ($\mu^+ + \mu^-$) at the L_3 edges and the degree of the X-ray polarization. A finite XMCD signal at 80 K indicates a weak ferromagnetic order in the manganese oxide nanosheets at low temperatures, which has been predicted in a first-principles calculation [5].

REFERENCES

1. N. Tombros, C. Jozsa, M. Popinciuc, H. T. Jonkman, and B. J. van Wees, *Nature* **448**, 571 (2007).
2. O. V Yazyev, *Rep. Prog. Phys.* **73**, 056501 (2010).
3. N. Saitou, Y. Hirano, M. Sawada, H. Namatame, M. Taniguchi, T. Taniguchi, Y. Matsumoto, and M. Hara, *J. Phys. Soc. Jpn.* **85**, 035002 (2016).
4. L. Wang, Y. Omomo, N. Sakai, K. Fukuda, I. Nakai, Y. Ebina, K. Takada, M. Watanabe, and T. Sasaki, *Chem. Mater.* **15**, 2873 (2003).
5. M. Kan, J. Zhou, Q. Sun, Y. Kawazoe, and P. Jena, *J. Phys. Chem. Lett.* **4**, 3382 (2013).

XMCD And XAS Study Of CoFeB Heterostructures Grown On Different Substrates For Spintronic Applications

Andrey K. Kaveev[a], Nikita S. Zhiltsov[a], Alexander M. Korovin[a] and Masahiro Sawada[b]

*[a] Ioffe Institute, 194021, 26 Polytechnicheskaya str., Saint-Petersburg, Russia*
[b] Hiroshima university, Hiroshima, Japan

Keywords: CoFeB, Laser Molecular Beam epitaxy, Spin, Orbital magnetic moment.

The existing interest to the thin layers of magnetic metallic alloys is related to various potential applications of these materials in spintronics, magnonics, etc. Especially attractive among those are three-component 3d-metallic and Heusler alloys because of high degree of spin polarization [1, 2]. This property plays an important role in development and fabrication of spin injection devices [3, 4]. These alloys are also very attractive for application in novel mass storage devices, such as Magnetic Tunnel Junction (MTJ) based Magnetic Random Access Memory (MRAM) [5], allowing high density and extended time stability information storage. The possibility to tune magnetic moment orientation of ferromagnetic (FM) layer by applying a relatively weak electric field can be realized in CoFeB/MgO/CoFeB based MTJs exhibiting the highest tunnel magnetoresistance (TMR) values [6]. On the other hand, studies of the ferromagnetic (FM, or ferromagnetic insulator) - TI interface are attractive due to the magnetic proximity effect, which acts as symmetry breaking factor relative to the topological states time inversion. This effect appears in FM exchange field influence on TI surface states. Therefore the studies of the ferromagnetic CoFeB grown on different substrates is of interest from the point of view of different practical applications.

We have grown and studied $Co_{40}Fe_{40}B_{20}$ (CoFeB in text) films using different substrates: Bi_2Se_3(0001), MgO(001), Fe_3O_4(001)/MgO(001) and GaN(0001). These layers were grown with use of laser MBE system (produced by Surface, GmbH.) based on KrF_6 excimer laser. Clear surface of Bi_2Se_3 substrates was obtained using adhesive tape to eliminate top layer of the material. To dehydrate the surface, Bi_2Se_3 substrates were annealed under 10^{-8} mBar pressure at 200°C during 30 minutes. The CoFeB layer was grown on the Bi_2Se_3 substrate in two ways: at RT directly, and on high temperature (400°C) 3-8 Å thick seeding layer with subsequent RT growth of 9-10 nm more. RHEED analysis was performed in-situ with use of built-in diffractometer at 30 kV. We have carried out an image analysis via special software developed in our group [6]. The software allows one to plot 3D projections of RHEED patterns in the reciprocal space for concrete zone axis. AFM measurements were realized with the microscope produced by NT-MDT (Zelenograd, Russia).

In case of growth CoFeB on Bi_2Se_3 direct growth of the material at elevated temperatures is impossible because of high chemical activity of Se. Nevertheless, very thin CoFeB layer demonstrates a set of streaks on a RHEED pattern (not shown here) showing an ordering. Further growth of CoFeB at RT allows us to obtain polycrystalline CoFeB layer (circles on a RHEED patterns). XAS and XMCD measurements of Co 2p edge (BL14 beamline, HiSOR, Hiroshima, Japan) shows metallic Co state in these layers (see Fig. 1).
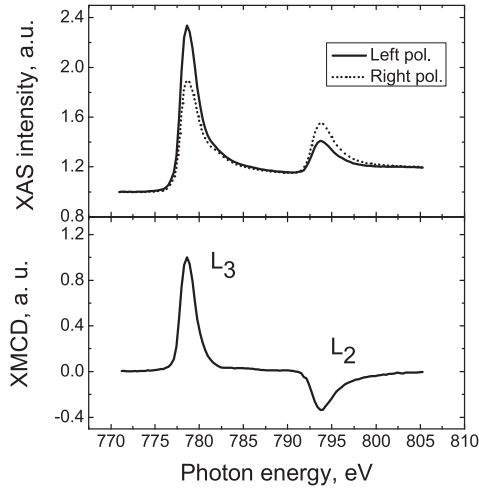
FIGURE 1. XAS (top) and XMCD signal (bottom) of Co 2p edge for CoFeB layer grown on Bi_2Se_3. Shape of curves corresponds to metallic Co state.
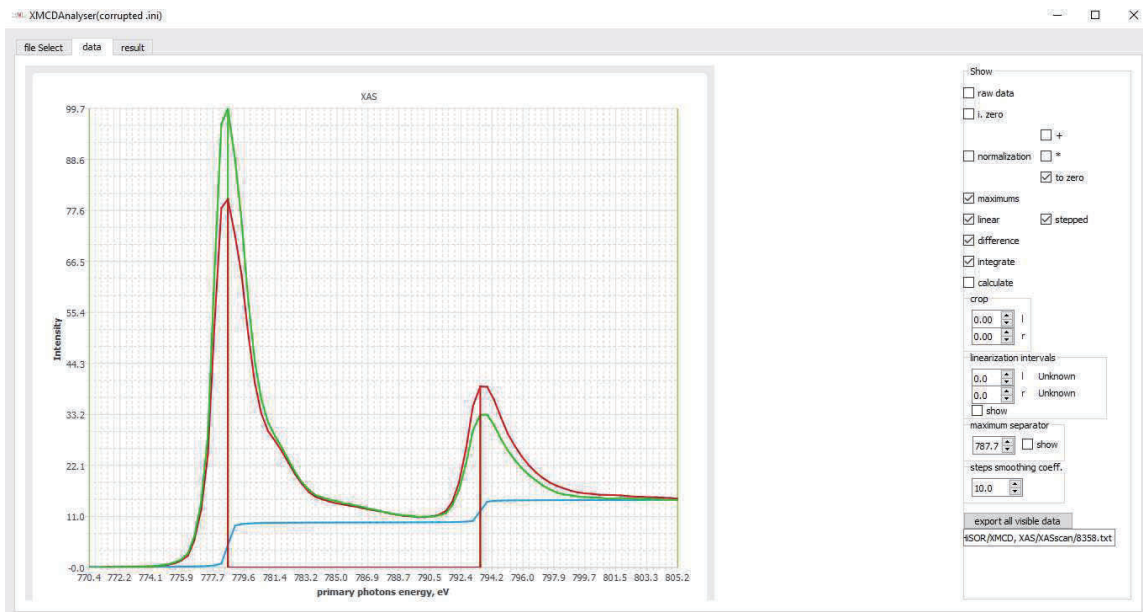
FIGURE 2. Screen of the software for sin and orbital moment calculation from XMCD integration data.

The same metallic Co and Fe states were observed in case of CoFeB growth on MgO, GaN and Fe_3O_4 on the basis of XAS spectra analysis.

Besides the metal state characterization using XAS spectra, one may calculate spin and orbital magnetic moments according to known sum rules [7]. To make this, the authors have written the software which allows such calculations. To date the work related to the numeric analysis of the obtained data goes on.

REFERENCES

1. L. Bainsla et al., J. Appl. Phys., Vol. 116, page 203902 (2014)
2. A. McNichol Boldin, Macalester Journal of Physics and Astronomy, Volume 3, Issue 1, art. 3 (2015)
3. J. Fabian et al., Acta physica slovaca, vol. 57 No. 4 & 5, 565 – 907 (2007)
4. J.F. Gregg et al.,, J. Magn. Magn. Mater., 265 (2003) 274–289
5. S. Parkin et al., Proc. IEEE, V. 91, N. 5, 661 (2003)
6. S. Pandharpure, "Process development for integration of CoFeB/MgO-based magnetic tunnel junction (MTJ) device on silicon" (2007). Thesis. Rochester Institute of Technology.
7. J Stohr, J. Magn. Magn. Mater., 200 (1999) 470-497

Nano-scale exchange coupling of antiferromagnetic Cr and ferromagnetic Ni thin film heterostructures

T. Miyamachi[a], S. Nakashima[a], M. Sawada[b], and F. Komori[a]

[a] *Institute for Solid State Physics, University of Tokyo, Kashiwa, Chiba 277-8581, Japan*
[b]*Hiroshima Synchrotron Radiation Center, Hiroshima University,
Higashi-Hiroshima, Hiroshima 739-0046, Japan*

Keywords: X-ray magnetic circular dichroism, thin film heterostructure, magnetic anisotropy

Thin film heterostructures composed of antiferromagnetic (AFM) and ferromagnetic (FM) layers attract great attention not only for their promising potentials for device applications, but also for fundamental interests in their structural, electronic and magnetic properties at the interface of AFM and FM layers. The strength of the magnetic coupling between AFM and FM layers relies on its interfacial conditions. Especially for the exchange energy, a considerable reduction of experimental values compared to theoretical ones with the ideal interface is reported. This difference could be attributed to the destabilization of interfacial magnetic structures caused by the roughness, intermixing, or alloying at the AFM/FM interface. Recently, we have demonstrated that the roughness or alloy composition at the AFM/FM interface, which determines electronic and magnetic properties of the FM layer, strongly depends on the thickness of the upper AFM layer [1]. Thus, investigations of structural, electronic and magnetic properties of the AFM/FM thin film heterostructures with different thicknesses of the AFM layer are essential to understand its intrinsic magnetic coupling.

In this study, we studied electronic and magnetic properties of Cr/Ni thin film heterostructures grown on a Cu(001) substrate by x-ray absorption spectroscopy/x-ray magnetic circular dichroism (XAS/XMCD). Ni thin films on Cu(001) as the FM layer exhibit so-called spin reorientation transition (SRT) from in-plan to out-of-plane easy magnetization at the critical thickness of about 7-10 monolayers (ML) [2,3]. Thus, near the transition thickness, the impact of the magnetic coupling with the AFM Cr layer as well as the interfacial structural changes could be detected as a shift of the easy magnetization direction. To fabricate Cr/Ni thin film heterostructures as schematically shown in Fig.1 (a), 6 ML Ni thin films with in-plane easy magnetization are first grown on Cu(001), and subsequently step-like growths of 1 and 5 ML Cr thin films using a wedge technique are proceeded at room temperature in ultrahigh vacuum. The XAS/XMCD measurements were performed at BL14 of HiSOR with B = 0, $\pm$ 0.3 T and T = 80 K. The spectra were recorded in the total electron yield mode in the normal (NI: $\theta = 0°$) and the grazing (GI: $\theta = 55°$) incidences. Note that θ is the angle between the sample normal and the incident x-ray. The XMCD is defined as $\mu_+ - \mu_-$, where μ_+ and μ_- denote XAS at the Ni and Cr $L_{2,3}$ adsorption edges with the photon helicity parallel and antiparallel to the sample magnetization.
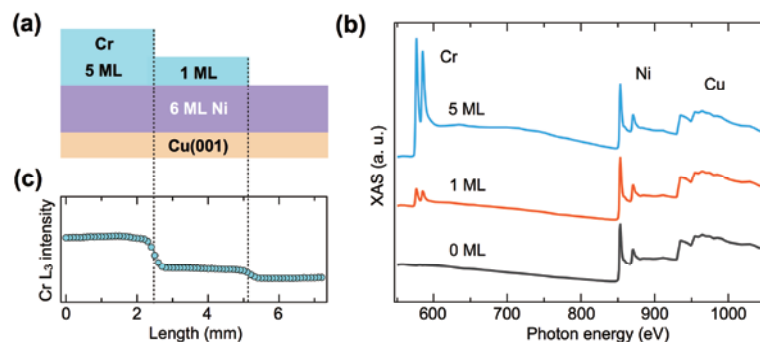
FIGURE 1. Structural characterizations of Cr/Ni thin film heterostructures. (a) A schematic of Cr/Ni thin film heterostructures. (b) XAS spectra of Cr, Ni and Cu $L_{2,3}$ absorption edges with 0, 1 and 5 ML Cr overlayers on 6 ML Ni/Cu(001) recorded at NI geometry. Note that each spectra is normalized by the edge jump intensity of the Cu $L_{2,3}$ region. (c) The plot of the Cr L_3 peak intensity across the sample.

Firstly, the sample quality is checked by XAS. Figure 1(b) displays XAS spectra of Cr, Ni and Cu $L_{2,3}$ absorption edges of Cr/Ni thin film heterostructures with different Cr thicknesses (Cr thickness: 0, 1 and 5 ML). The proportional increase in the Cr $L_{2,3}$ edge jump intensity relative to Ni one is clearly seen with increasing thickness of the Cr overlayer. Comparable Ni $L_{2,3}$ edge jump intensity at each region The homogeneity of Cr/Ni thin film heterostructures is conformed by comparable Ni $L_{2,3}$ edge jump intensity with 0, 1 and 5 ML Cr overlayers, and further by the plot the Cr L_3 peak intensity across the sample as shown in Fig. 1(c). Nearly constant behaviors of the Cr L_3 peak intensity at each region ensure the high sample quality.

Magnetic properties of structurally controlled Cr/Ni thin film heterostructures are investigated by XMCD. Figure 2(a) displays XAS and remanent ($\pm\,0.3 \rightarrow 0$ T) XMCD reference spectra of the bare 6 ML Ni/Cu(001). As previously reported [2,3], a much larger XMCD signal at GI geometry than NI geometry is clearly observed, revealing the in-plane easy magnetization of Ni thin films at this thickness. The impact of additional Cr overlayers on the easy magnetization direction is discussed from the comparison of magnetization curves of the 6 ML Ni/Cu(001) with 0, 1 and 5 ML Cr overlayers. The magnetization curves are obtained at GI and NI geometries by plotting the Ni L_3 peak intensity normalized by the pre-edge one by sweeping an external magnetic field [4]. We find from the magnetization curves shown in Fig. 2 (b) that, with increasing the thickness of Cr overlayers, the remanent magnetization and coercivity decrease at GI geometry while the magnetization by the external magnetic field increases at NI geometry. At 5 ML Cr overlayers, the magnetization at GI geometry at available maximum magnetic fields of $\pm\,0.3$ T is comparable to that at NI geometry. These results indicate that adding Cr overlayers lowers the in-plane magnetic anisotropy of the 6 ML Ni/Cu(001), which could be attributed to the magnetic coupling induced change in the magnetic anisotropy or structural modifications such as enhanced roughness, intermixing, or alloying at the AFM/FM interface. In future work, together with atomic scale surface and interface characterizations by scanning tunneling microscopy, XAS/XMCD measurements using thicker Ni thin films with out-of-plane easy magnetization will be performed, giving a deeper understanding of the magnetic coupling at the interface of Cr/Ni thin film heterostructures.
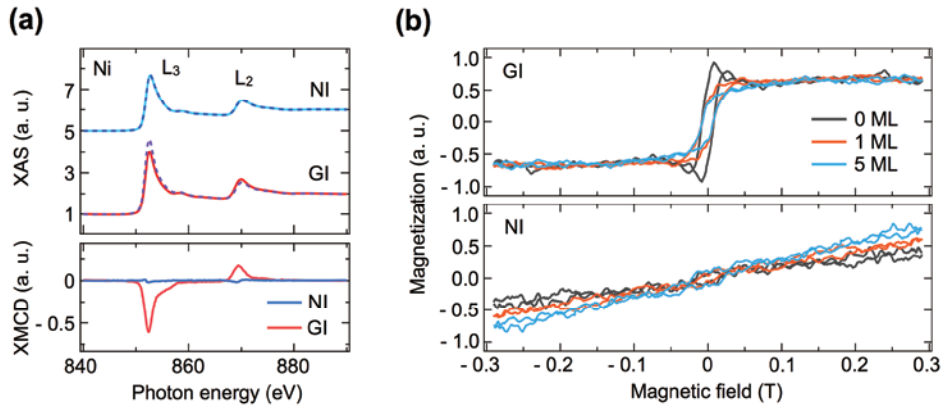
FIGURE 2. Magnetic properties of Cr/Ni thin film heterostructures. (a) Ni $L_{2,3}$ edge XAS and remanent XMCD spectra of bare 6 ML Ni/Cu(001) at NI and GI geometries. Solid and dashed XAS spectra represent μ_+ and μ_-, respectively. (b) Magnetization curves of Cr/Ni thin film heterostructures with 0, 1 and 5 ML Cr overlayers recorded at GI (upper panel) and NI (lower panel) geometries. The Ni L_3 peak intensity normalized by the pre-edge one is plotted.

REFERENCES

1. S. Nakashima *et al.*, *submitted.*
2. B. Schulz and K. Baberschke, Phys. Rev. B **50**, 13467 (1994).
3. W. L. O'Brien and B. P. Tonner, Phys. Rev. B **49**, 15370 (1994).
4. E. Goering *et al.*, J. Appl. Phys. **10**, 5920 (2000).

XMCD study of magnetic proximity effect in Co (Ni) / $Y_3Fe_5O_{12}$ heterostructures

N.S. Sokolov[a], A.M. Korovin[a], S.M. Suturin[a], M.Sawada[b]

[a] *Ioffe Institute, 194021, 26 Polytechnicheskaya str., Saint-Petersburg, Russia*
[b] *Hiroshima Synchrotron Radiation Center, Hiroshima, Japan*

Keywords: YIG, GGG, Co, Laser Molecular Beam epitaxy, exchange bias.

Yttrium iron garnet is a well-known material due to its unique physical properties such as the exclusively narrow ferromagnetic resonance line, high optical and acoustic transparency and high Curie temperature (Tc = 560 K). Cobalt is a widely used 3d magnetic metal showing a large value of magnetic moment (4πMs ~ 18 kG) and elevated Curie temperature (Tc = 1121°C). The aim of the present study is to clarify the main features of the exchange interaction in Co / GGG / YIG heterostructures.

The samples were grown on $GGG(Ga_5Gd_3O_{12})$ (111) substrates by laser molecular beam epitaxy. To make the initial surface atomically flat, the GGG substrates were annealed prior to growth for 3 hours at 1000°C in ambient air conditions. YIG ($Y_3Fe_5O_{12}$) ferrimagentic layers having thickness of 25 nm as well as GGG non-magnetic spacer layers having thickness of 0.5-3 nm were deposited in oxygen at 850°C by ablating the corresponding targets. The layer-by-layer growth of YIG and GGG was monitored in-situ by RHEED using the specular beam intensity oscillations as a measure of the layer thickness. Atomic force microscopy measurements performed on the annealed GGG substrate surface as well as on the surface of the deposited YIG and GGG layers showed atomically smooth terraces separated by ~1.8 Å steps, the step height corresponding well to the distance between adjacent (111) layers in the garnet crystal structure.

The cobalt layer having thickness of 1-3 nm was grown at 100°C on the garnet surface by ablating Co target in UHV conditions, which resulted in polycrystalline film as evidenced by RHEED. Co layer shows interconnected islands with diameters below 10 nm. The height variation in the topography images is under 0.6 nm with a surface rms-roughness of about 0.2 nm.

The magnetic properties of the grown multilayers were investigated by visible light and X-ray magneto-optical methods. Longitudinal Kerr effect (LMOKE) measurements were performed at multiple wavelengths (λ = 633 nm, 535 nm and 405 nm) to distinguish contributions of Co and YIG layers with magnetic field oriented parallel and perpendicular to the light incidence plane. The element selective X-ray magnetic circular dichroism (XMCD) studies were performed across Fe and Co L_{23} edges at BL14 beamline (HiSOR Synchrotron Radiation Center, Hiroshima University).
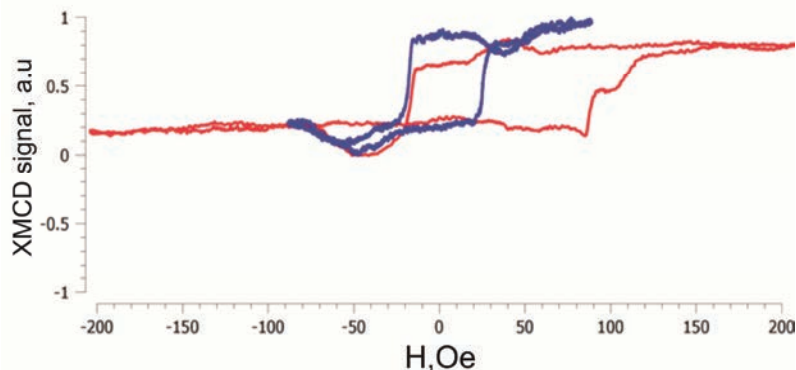
FIGURE 1. Hysteresis loops measured on Fe edge in Co/GGG/YIG/GGG(111) before (blue) and after applying magnetic field pulse comparable to the cobalt layer coercivity

Interestingly when Co and YIG layers are combined in the same heterostructure the magnetization behavior becomes strongly dependent on whether the layers are in direct contact or separated by a thin GGG spacer. In Co / GGG / YIG multilayers the coercive field of YIG layer is not much changed with respect to the stand alone YIG layers, however the hysteresis loop gets horizontally shifted by up to 10 Oe if measured after applying a magnetic field pulse comparable to the cobalt layer coercivity. The pulse is supposed responsible for the sign switching of the Co layer remanent magnetization that in turn induces the YIG hysteresis loop bias. The effect of Co layer is additive, i.e. the YIG layer effectively feels the sum of the external field and the field generated by the Co remanent magnetization. The exchange bias of the YIG magnetization loop in Co / GGG / YIG heterostructures was confirmed by element selective synchrotron XMCD measurements (Fig. 1) conducted at Fe L_{23} absorption edge at E = 710 eV.

In contrast, Co/YIG heterestructures without GGG spacer have no YIG hysteresis loops shift. YIG loops have the same coercivity as Co loops (Fig. 2). YIG loops coercivity in such heterestructure is much bigger then coercivity of bulk YIG. Any kind of sample demagnetization or big field pulses applying cannot uncouple Co and YIG loops. These results confirm the previously obtained data on the presence of proximity effect in Co/YIG heterostructures [1].
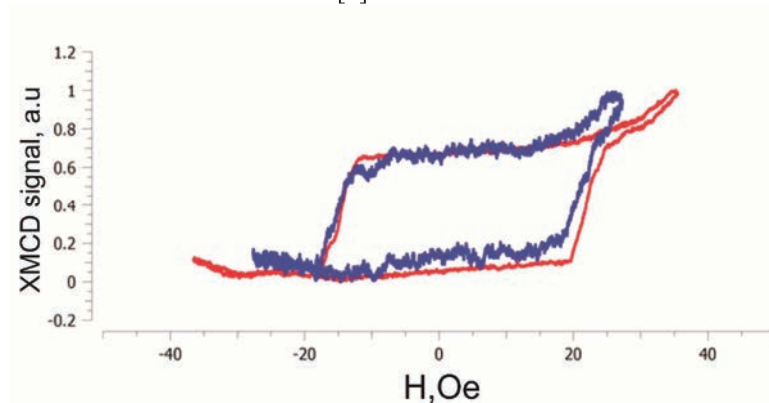
FIGURE 2. Hysteresis loops measured at Co (red) and Fe (blue) edges from Co/YIG/GGG(111) heterostructure.

In conclusion, we have observed that the magnetic layers in the Co / GGG / YIG nanostructures are coupled by interlayer exchange interaction manifesting itself in exchange bias of YIG magnetization curves. This gives rise to manipulation of YIG magnetization by change of Co remanence in external magnetic field. Exchange interaction can also give rise to orthogonal orientation of YIG and Co magnetizations due to biquadratic coupling analogous to that observed earlier in Fe/Cr/Fe structures [2].

REFERENCES

[1] V. V. Fedorov, S. V. Gastev, A. M. Korovin, Yu. Yu. Petrova, S. M. Suturin, M. Sawada and N. S.Sokolov. Proc. 23rd Int. Symp. "Nanostructures: Physics and Technology" St. Petersburg, Russia, June 22–26, 2015, p.126

[2] J. C. Slonczewski, Phys. Rev. Lett. 67, 3172 (1991); J. Appl. Phys. 73, 5957 (1993); J. Magn. Magn. Mater. 150, 13 (1995).